https://doi.org/10.5194/egusphere-2026-2144
Preprint. Discussion started: 22 April 2026

A wind-farm wake-turbulence parameterization for the WRF model (EWP v2.0)

Oscar García-Santiago[1], Jake Badger[1], Andrea N. Hahmann[1], Patrick J. H. Volker[2], Søren Ott[1], M. Paul van der Laan[1], and Mark Kelly[1]

[1]Department of Wind and Energy Systems, Technical University of Denmark, Roskilde, Denmark

Correspondence: Oscar García-Santiago (osmasa@dtu.dk)

Abstract.

Wind farm parameterizations are essential components of mesoscale models used to assess the impact of wind farm operation on the atmospheric flow and surface climate. These models represent wind turbines as momentum sinks and sources of turbulence. We describe the theoretical basis and implementation of an improved model to enhance the Turbulent Kinetic Energy (TKE) treatment in wind farm parameterizations. The novel Latent Kinetic Energy (LKE) model integrates the tracer capabilities of the Weather Research and Forecasting (WRF) model to accurately account for wind turbine-generated TKE throughout the wakes in and downwind of wind farms. The formulation is compatible with multiple 1.5-order planetary boundary layer (PBL) schemes in the WRF model and is implemented within the explicit wake parameterization. We evaluate the LKE model against WRF large-eddy simulations with actuator-disc representations of wind turbines for an idealized 6×6 wind farm and for three 1.5-order PBL schemes. The LKE formulation improves the representation of wake turbulence, reducing normalized TKE differences relative to the large-eddy simulations to within 15 % over the wind farm region. In contrast, the Fitch wind farm parameterization with default parameter values shows 40 %. The results further show that PBL-specific calibration is required; with appropriate calibration, the LKE approach maintains normalized TKE differences within 15 % and reproduces the hub-height wind-speed deficit within 1 % of the reference.

1 Introduction

The rapid expansion of wind farms globally, driven by the increasing demand for clean and sustainable energy, requires a thorough understanding of their impacts on the atmosphere (Veers et al., 2019). Previous research shows that wind energy extraction on a large scale can significantly change near-surface conditions and the atmospheric boundary layer (ABL), altering its depth and wind direction (Allaerts and Meyers, 2017; Lanzilao and Meyers, 2022; Maas and Raasch, 2022). This highlights the importance of considering the two-way interaction between wind farms and the ABL, as atmospheric conditions also affect turbine energy production (Porté-Agel et al., 2020). This bidirectional relationship is critical not only in the planning but also in the operational phases of wind farm projects. Therefore, atmospheric models that can capture these interactions are crucial for assessing the impact of wind farms on local wind resources and vice versa, considering their significant economic and environmental implications (Lundquist et al., 2019; Akhtar et al., 2021).

https://doi.org/10.5194/egusphere-2026-2144
Preprint. Discussion started: 22 April 2026

The representation of wind farms in atmospheric models has evolved significantly from initially simulating wind farms as areas of increased surface roughness or drag in global and regional climate models, to more sophisticated parameterizations in mesoscale models (Pan and Archer, 2018; Fischereit et al., 2022). These later parameterizations represent wind turbines as elevated (i.e., above the surface) momentum sinks and turbulent kinetic energy (TKE) sources. The Weather Research and Forecasting (WRF; Skamarock et al., 2021) model has emerged as one of the preferred mesoscale models for implementing and applying such wind farm parameterizations (Fischereit et al., 2022). However, integrating explicit TKE sources into the WRF model requires using planetary boundary layer schemes capable of predicting TKE.

Planetary boundary layer (PBL) schemes in atmospheric models are crucial in modelling vertical turbulent processes that influence temperature, moisture, and momentum throughout the atmospheric column. Among these schemes implemented in the WRF model, the 1.5-order PBL schemes can prognose TKE and manage TKE columns independently. However, exceptions, one being the Mellor-Yamada Nakanishi Niino (MYNN; Nakanishi and Niino, 2009) scheme, further incorporate TKE advection.

The wind farm parameterization (WFP) proposed by Fitch et al. (2012), commonly known as the Fitch parameterization, stands out as the most widely adopted WFP in the WRF model, mainly due to its integration into the model's public releases (Fischereit et al., 2022). This parameterization incorporates an explicit TKE source and makes use of the TKE advection feature to transport TKE downstream. TKE advection is essential, as it allows the TKE "injected" by wind turbines to properly mix with the atmosphere at the scale of the mesoscale model, preventing spurious TKE accumulation at turbine-containing grid cells. Consequently, WRF model studies employing the Fitch parameterization predominantly use the MYNN PBL scheme. This, however, imposes a severe limitation by restricting simulations to a single PBL scheme.

The WRF model sensitivity to PBL scheme selection is well documented (Draxl et al., 2014; Carvalho et al., 2014; Hahmann et al., 2020; Bodini et al., 2023), along with the impact of other factors such as grid resolution (Skamarock, 2004; Olsen et al., 2017; Floors et al., 2018). Given the variability in performance across different regions and case studies, there is no universally optimal PBL scheme. This variability poses challenges, particularly when the MYNN scheme, perhaps well-suited for integrating wake effects from WFPs, may not be the best choice for a specific region or case requiring wake effect assessment. In addressing this, recent research by Rybchuk et al. (2022) and Peña et al. (2023) explored implementing the Fitch parameterization within an alternative PBL scheme, the NCAR 3DPBL (Kosović et al., 2020; Juliano et al., 2022), beyond the commonly used MYNN scheme. This investigation contributed to understanding how the choice of the PBL scheme influences the modelled mesoscale wake and its impact on the atmosphere.

An alternative approach to exploring wind farm effects under different PBL schemes is to shift focus away from the explicit TKE sources in wind farm parameterizations. The Explicit Wake parameterization (EWP; Volker et al., 2015) is a WFP in the WRF model that, unlike the Fitch parameterization, does not explicitly incorporate a TKE source; instead, TKE contributions from wind turbines are implicitly generated through increased shear associated with wakes—and without a change in buoyancy, shear and TKE decrease below and increase above hub height compared to up-wind conditions. However, performance with other PBL schemes has not been established, as EWP has only been applied with the MYNN scheme.

https://doi.org/10.5194/egusphere-2026-2144
Preprint. Discussion started: 22 April 2026

The methodological differences between the EWP and Fitch parameterization lead to some systematic differences in simulation results (Shepherd et al., 2020; Pryor et al., 2022). Generally, studies evaluating EWP indicate that shear-generated TKE underestimates the reference simulations and measurements, suggesting an explicit TKE source of some kind is probably needed (Larsén and Fischereit, 2021; Ali et al., 2023; García-Santiago et al., 2024). In contrast, initial applications of the Fitch parameterization showed TKE overestimation (Abkar and Porté-Agel, 2015; Siedersleben et al., 2020). This overestimation was attributed to a coding error and an excessively large TKE source, issues rectified by Archer et al. (2020). However, even after correction, the spatial structure of the added TKE, as shown in Large-Eddy Simulations (LES), only partially matches *further downstream* of turbines, and requires a relatively large TKE source at *turbine locations* (Archer et al., 2020; Peña et al., 2022; García-Santiago et al., 2024).

This article presents a novel approach within the EWP framework to address issues related to explicit TKE sources that significantly improve the TKE representation. Referred to hereafter as the Latent Kinetic Energy (LKE) model, this new approach utilises the tracer capability of the WRF model to better simulate TKE at the turbine's location and throughout the wake's evolution. Notably, the LKE model integrates TKE advection into the EWP framework, making it independent of the MYNN PBL scheme and thus compatible with other 1.5-order PBL schemes. We evaluated the LKE model (implemented in the EWP) and the Fitch parameterization against LES with actuator discs (AD), focusing on the streamwise development of TKE to assess the performance of the new approach in simulating an idealised offshore wind farm in the same way as done in García-Santiago et al. (2024) (hereinafter referred as GS2024).

In Sect. 2, we derive the theoretical basis of the LKE model and its implementation in the EWP within the WRF model. Section 3 presents the WRF model configuration for the LES and mesoscale simulations, the wind farm parameterizations, and the methods used for comparison. In Sect. 4 to 6, the LKE model is compared to other wind farm parameterizations and evaluated against the LES results. Finally, Sections 7 and 8 discuss our results and summarise the key conclusions of the study.

2 The latent kinetic energy concept

We introduce a novel model within the EWP to integrate TKE contributions from wind turbines into the 1.5-order PBL schemes. This model addresses the current shortcomings in handling TKE in wind farm parameterizations by incorporating terms in the TKE equations of PBL schemes that arise from the effects of "double averaging" (both ensemble and spatial) on the non-homogeneous sub-grid scale flows in each grid cell. Our theoretical foundation relies on the work of Raupach and Shaw (1982) and Volker et al. (2015), subsequently referred to as RS1982 and V2015. In the following (sub-)sections, we present the relevant mesoscale model equations, the development of the new TKE model, and their implementations in the WRF model.

2.1 Background

Turbulent fluxes in mesoscale models are typically parameterized only in the vertical direction due to the coarse horizontal resolution (Mellor and Yamada, 1982). Consequently, in standard 1.5-order closure PBL schemes, the TKE budget equation is

https://doi.org/10.5194/egusphere-2026-2144
Preprint. Discussion started: 22 April 2026

simplified as

$$\frac{\partial \bar{k}}{\partial t} = \bar{\mathcal{P}}_\mathrm{s} + \bar{\mathcal{P}}_\mathrm{b} + \bar{\mathcal{T}}_\mathrm{t} - \bar{\epsilon}\,. \tag{1}$$

where the left-hand side represents the temporal evolution of TKE, $\bar{k} = \overline{u_i' u_i'}/2$. Here, u_i denotes the velocity components ($i = 1, 2, 3$), primes denote fluctuations about the ensemble mean, and the overbar denotes ensemble averaging. The terms on the right-hand side represent shear production ($\bar{\mathcal{P}}_\mathrm{s}$), buoyant production ($\bar{\mathcal{P}}_\mathrm{b}$), transport of TKE ($\bar{\mathcal{T}}_\mathrm{t}$), and dissipation ($\bar{\epsilon}$). In this one-dimensional PBL formulation, advection is omitted. Because unresolved turbulence is treated independently within each vertical column, lateral heterogeneity associated with sub-grid flow structures is not explicitly represented. Thus, the ensemble-averaged quantities in Eq. (1) are assumed to be horizontally homogeneous at the sub-grid scale (Wyngaard, 1992).

Including wind turbines in such schemes challenges this assumption of spatial homogeneity, because the unresolved turbine wake within a grid cell constitutes a spatial perturbation to the homogeneous mean flow. To identify the contributions of wind turbines and their wakes to the PBL TKE equation (Eq. 1), we derive a TKE budget equation that accounts for flow in the presence of sub-grid elements. This is accomplished by applying the double-averaging procedure outlined by RS1982 (see Appendix A). Starting from the momentum conservation equation (Eq. A3), which includes a forcing term f_i associated with the action of the wind turbines, we obtain the spatially averaged TKE budget equation (Eq. A7):

$$\frac{\partial \langle \bar{k} \rangle}{\partial t} = \langle \bar{\mathcal{P}}_\mathrm{s} \rangle + \langle \bar{\mathcal{P}}_\mathrm{w} \rangle + \langle \bar{\mathcal{P}}_\mathrm{b} \rangle + \langle \bar{\mathcal{P}}_\mathrm{f} \rangle + \langle \bar{\mathcal{T}}_\mathrm{t} \rangle + \langle \bar{\mathcal{T}}_\mathrm{w} \rangle - \langle \bar{\epsilon} \rangle\,, \tag{2}$$

where angle brackets denote spatial averaging. Equation (2) resembles those in RS1982, Finnigan (2000), and Finnigan and Shaw (2008); it further adds a turbine-induced TKE term, $\langle \bar{\mathcal{P}}_\mathrm{f} \rangle = \left\langle \overline{u_i' f_i'} \right\rangle$, and neglects advection for consistency with the 1D formulation of the PBL schemes.

Equation (2) also contains the wake production term $\langle \bar{\mathcal{P}}_\mathrm{w} \rangle$ and the dispersive transport term $\langle \bar{\mathcal{T}}_\mathrm{w} \rangle$, both of which emerge from the double-averaging procedure. These terms, together with $\langle \bar{\mathcal{P}}_\mathrm{f} \rangle$, represent the additional contributions from the turbines and their wakes introduced by the double averaging. Among them, V2015 found $\langle \bar{\mathcal{P}}_\mathrm{f} \rangle$ to be negligible, while RS1982 and Finnigan (2000) noted that $\langle \bar{\mathcal{T}}_\mathrm{w} \rangle$ is often neglected. Under these assumptions, the wake production term $\langle \bar{\mathcal{P}}_\mathrm{w} \rangle$ remains the primary missing source of turbine-induced TKE which can be represented in the PBL closure as an additional source term:

$$\frac{\partial \bar{k}}{\partial t} = \bar{\mathcal{P}}_\mathrm{s} + \bar{\mathcal{P}}_\mathrm{b} + \bar{\mathcal{T}}_\mathrm{t} - \bar{\epsilon} + \mathcal{S}_\mathrm{wt}, \tag{3}$$

where $\mathcal{S}_\mathrm{wt}$ is a parameterization guided by the wake-production term $\langle \bar{\mathcal{P}}_\mathrm{w} \rangle$ from the double-averaged framework.

2.1.1 Diagnosing wake production from kinetic energy budgets

The wake production term is given by

$$\langle \bar{\mathcal{P}}_\mathrm{w} \rangle = -\left\langle \overline{u_i' u_j'}'' \frac{\partial \bar{u}_i''}{\partial x_j} \right\rangle,$$

where double primes indicate spatial deviations (or *dispersive*, a term used in canopy studies) from the spatial mean, defined as $\bar{\phi}'' = \bar{\phi} - \langle \bar{\phi} \rangle$ for any ensemble-averaged variable $\bar{\phi}$ (Finnigan and Shaw, 2008). When the spatial average $\langle \cdot \rangle$ is interpreted

https://doi.org/10.5194/egusphere-2026-2144
Preprint. Discussion started: 22 April 2026

over a mesoscale grid cell, this term depends on unresolved spatial variations in the Reynolds stress and dispersive velocity field, which therefore require parameterization.

Under the double-averaging framework, the wake-production term $\langle \bar{\mathcal{P}}_{\mathrm{w}} \rangle$ transfers kinetic energy from the spatially heterogeneous mean flow to turbulence (Raupach and Shaw, 1982; Finnigan, 2000; Brunet, 2020). In this sense, it plays a role analogous to shear production, which transfers energy from the mean flow to turbulent fluctuations. The main idea is to model a leading-order portion of the mean kinetic energy budget to obtain $\langle \bar{\mathcal{P}}_{\mathrm{w}} \rangle$ (here, a sink) and then introduce this term as a source in the PBL TKE equation (Eq. 3).

The spatially averaged mean kinetic energy, $\frac{1}{2}\langle \bar{u}_i \bar{u}_i \rangle$, can be decomposed into the kinetic energy of the spatially averaged flow and that associated with spatial deviations from it (see Appendix A):

$$\frac{1}{2}\langle \bar{u}_i \bar{u}_i \rangle = \frac{1}{2}\langle \bar{u}_i \rangle \langle \bar{u}_i \rangle + \frac{1}{2}\langle \bar{u}_i'' \bar{u}_i'' \rangle . \tag{4}$$

The second term in the right-hand side represents the kinetic energy of the spatially heterogeneous ensemble-averaged flow field. Mesoscale models with PBL schemes only deals with two kinetic energy types : the kinetic energy of the grid-cell mean flow, corresponding to the first term on the right-hand side of Eq. (4), and the TKE, whereas kinetic energy associated with unresolved spatial deviations is not represented.

Within the double-averaging framework, separate budget equations can be derived for each term on the right-hand side of Eq. (4). The term $\langle \bar{\mathcal{P}}_{\mathrm{w}} \rangle$ appears in both the budget of $\frac{1}{2}\langle \bar{u}_i'' \bar{u}_i'' \rangle$ and the TKE budget, but with opposite sign. Physically, $\langle \bar{\mathcal{P}}_{\mathrm{w}} \rangle$ represents the progressive conversion of wake-induced, spatially coherent motions into turbulence as the wake mixes with the surrounding flow (Raupach and Shaw, 1982; Finnigan, 2000; Brunet, 2020).

In the following, we refer to $\frac{1}{2}\langle \bar{u}_i'' \bar{u}_i'' \rangle$ as *latent kinetic energy* (LKE), to emphasize that this budget is not directly represented by the turbulent mixing in the PBL closure until it is converted into TKE through $\langle \bar{\mathcal{P}}_{\mathrm{w}} \rangle$.

The LKE budget equation has the following form (see Appendix A for details):

$$\begin{aligned}
\frac{\partial}{\partial t}\left(\frac{1}{2}\langle \bar{u}_i'' \bar{u}_i'' \rangle\right) = & \underbrace{-\langle \bar{u}_j \rangle \frac{\partial \frac{1}{2}\langle \bar{u}_i'' \bar{u}_i'' \rangle}{\partial x_j}}_{\langle \bar{\mathcal{A}}_{\mathrm{d}} \rangle} \underbrace{-\langle \bar{u}_i'' \bar{u}_j'' \rangle \frac{\partial \langle \bar{u}_i \rangle}{\partial x_j}}_{\langle \bar{\mathcal{P}}_{\mathrm{d}} \rangle} + \underbrace{\left\langle \overline{u_i' u_j'}'' \frac{\partial \bar{u}_i''}{\partial x_j} \right\rangle}_{\langle \bar{\mathcal{P}}_{\mathrm{w}} \rangle} \\
& \underbrace{-\frac{\partial}{\partial x_j}\left(\left\langle \bar{u}_i'' \overline{u_i' u_j'}'' \right\rangle + \frac{\langle \bar{u}_i'' \bar{u}_i'' \bar{u}_j'' \rangle}{2} \right)}_{\langle \bar{\mathcal{T}}_{\mathrm{d}} \rangle} \underbrace{-\left\langle \frac{\bar{u}_i''}{\rho} \frac{\partial \bar{p}''}{\partial x_i} \right\rangle}_{\langle \bar{\mathcal{C}}_{\mathrm{d}} \rangle} \\
& \underbrace{-\delta_{i3} \frac{g}{\theta_0} \langle \bar{u}_i'' \bar{\theta}'' \rangle}_{\langle \bar{\mathcal{B}}_{\mathrm{d}} \rangle} \underbrace{+\nu \left\langle \bar{u}_i'' \frac{\partial^2 \bar{u}_i''}{\partial x_j \partial x_j} \right\rangle}_{\langle \bar{\mathcal{D}}_{\nu} \rangle} + \underbrace{\langle \bar{u}_i'' \bar{f}_i'' \rangle}_{\langle \bar{\mathcal{F}}_{\mathrm{d}} \rangle},
\end{aligned} \tag{5}$$

where p is the pressure, ρ is the density, and ν is the kinematic viscosity, δ_{i3} is the Kronecker delta, g the gravitational acceleration, θ is the potential temperature with subscript 0 indicating a reference state. Equation (5) is similar to that obtained by RS1982, but with the addition of the turbine-induced production rate $\langle \bar{u}_i'' \bar{f}_i'' \rangle$. Furthermore, RS1982 also provided that in

https://doi.org/10.5194/egusphere-2026-2144
Preprint. Discussion started: 22 April 2026

steady advection-free conditions, neglecting viscous terms (high Reynolds-number assumption), the budget for canopy flows can simply be reduced to a balance between $\langle \bar{\mathcal{P}}_\mathrm{w} \rangle$ and $\langle \bar{\mathcal{F}}_\mathrm{d} \rangle$.[1]

2.1.2 LES-based diagnosis of the LKE budget

To provide context for the magnitude and behaviour of the terms in Eq. 5, in flow around wind turbines, we diagnose the budget contributions from time-averaged LES output of a single wind turbine under neutral atmospheric conditions from GS2024. For a streamwise analysis, spatial averages and deviations are defined over a fixed square area in the y–z plane spanning the rotor. The resulting quantities should be interpreted as cross-sectional diagnostics of the LKE budget. Because the averaging area is finite and taken in the y–z plane, this averaging operation commutes with streamwise differentiation only. All terms in Eq. (5) were evaluated from this area-averaged definition except for the pressure-related contributions and the turbine-induced term $\langle \bar{\mathcal{F}}_\mathrm{d} \rangle$, as p and f_i were unavailable. These missing contributions are therefore represented by the residual R of the diagnosed budget.

Figure 1a shows the streamwise evolution of the LKE budget terms. Close to the rotor, the residual is positive and dominant, indicating that the turbine forcing (with pressure contributions) is the principal contributor to LKE production in this region. The dispersive Reynold stresses production $\langle \bar{\mathcal{P}}_\mathrm{d} \rangle$ and the transport term $\langle \bar{\mathcal{T}}_\mathrm{d} \rangle$ also contribute positively, although with smaller magnitude than the residual. Downstream (approximately $3D_0$), production decreases, and the wake production $\langle \mathcal{P}_\mathrm{w} \rangle$ becomes the primary sink downstream of the turbine followed by the transport term.

The behaviour of $\langle \mathcal{P}_\mathrm{w} \rangle$ is examined in more detail in Fig. 1b. When scaled by an appropriate factor, $\langle \mathcal{P}_\mathrm{w} \rangle$ closely resembles the streamwise evolution of LKE, suggesting that the depletion of LKE by $\langle \bar{\mathcal{P}}_\mathrm{w} \rangle$ is inversely proportional to a characteristic time scale.

These comparisons are intended as a qualitative diagnostic; a complete budget analysis requires an additional dedicated study. Regardless, these patterns provide useful guidance for constructing a simplified prognostic LKE model. The following section introduces such model for mesoscale applications, including parameterizations of $\langle \bar{\mathcal{P}}_\mathrm{w} \rangle$ and the relevant source terms.

2.2 The tracer-based parameterization

To represent the LKE budget in mesoscale modeling, we propose the use of a prognostic scalar with sources and sinks corresponding to those in the LKE budget derived above. Let

$$C(x_j, t) \equiv \tfrac{1}{2} \langle \bar{u}_i'' \bar{u}_i'' \rangle \tag{6}$$

denote a scalar that represents the LKE per unit mass for a given grid cell, with units of $\mathrm{m}^2\,\mathrm{s}^{-2}$. Such scalar is transported by the resolved flow $\langle \bar{u}_i \rangle$ and diffused by an eddy diffusivity $K_h(x_j, t)$, similar for other scalars. Motivated from the behaviour of $\langle \bar{\mathcal{P}}_\mathrm{w} \rangle$ relative to $\frac{1}{2}\langle \bar{u}_i'' \bar{u}_i'' \rangle$ in Sect. 2.1.2, and again neglecting viscous contributions, we formulate the leading-order prognostic

[1] Notice that in RS1982 the term $\langle \bar{\mathcal{F}}_\mathrm{d} \rangle$ is represented by $\frac{1}{\rho} \langle \bar{u}_i \rangle \left\langle \frac{\partial \bar{p}''}{\partial x_i} \right\rangle$, a term derived from $\left\langle \frac{\bar{u}_i''}{\rho} \frac{\partial \bar{p}''}{\partial x_i} \right\rangle$.

https://doi.org/10.5194/egusphere-2026-2144
Preprint. Discussion started: 22 April 2026

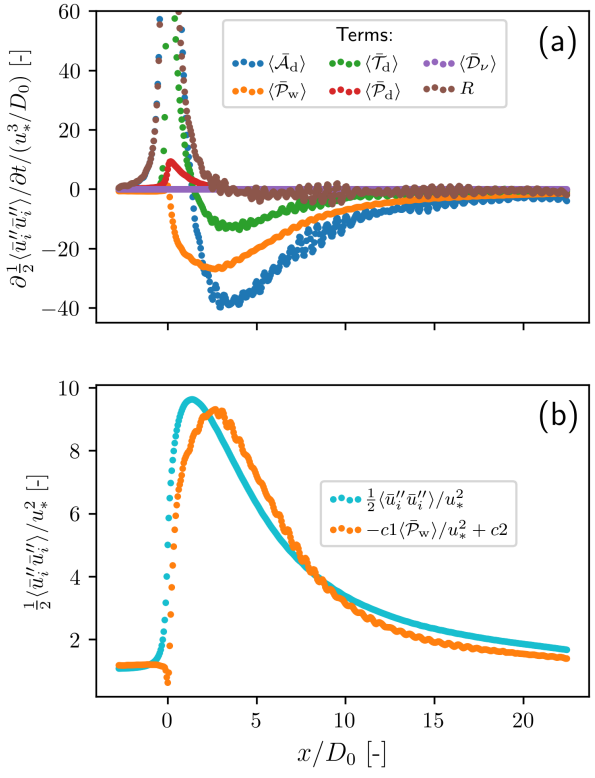

Figure 1. Streamwise evolution of (a) LKE budget terms in Eq. (5) with a residual R and (b) only showing $\frac{1}{2}\langle \bar{u}_i'' \bar{u}_i'' \rangle$ and $\langle \bar{\mathcal{P}}_\mathrm{w} \rangle$ with values of $c_1 = 200\,\mathrm{s}$ and $c_2 = 1$. Terms are computed from LES outputs of a single wind turbine under neutral conditions (GS2024). Spatial averages are taken over a y–z plane spanning the turbine rotor.

equation for C in the (non-conservative) form

$$\frac{\partial C}{\partial t} + \langle \bar{u}_i \rangle \frac{\partial C}{\partial x_i} - \frac{\partial}{\partial x_i}\left(K_h \frac{\partial C}{\partial x_i} \right) = -\lambda C + Q; \tag{7}$$

the left-hand side is handled by mesoscale models with tracer capabilities (e.g. the WRF model). The advection and diffusion of C resembles the advection and transport terms in Eq. (5). In this framework, the transport term in Eq. (5) is interpreted as a gradient-diffusion flux of C which should use an effective eddy diffusivity K_C. For consistency (and pragmatism) with the scalar-mixing operator of the mesoscale model, we use $K_C \approx K_h$.

The right-hand side of Eq. (7) parameterizes the dominant subgrid processes. The term $-\lambda C$ represents the sink associated with $\langle \bar{\mathcal{P}}_\mathrm{w} \rangle$, where the effective decay rate λ needs parameterization; the term Q collects the remaining source contributions (e.g. turbine-induced production).

https://doi.org/10.5194/egusphere-2026-2144
Preprint. Discussion started: 22 April 2026

2.2.1 Parameterization of the LKE decay rate λ

A first choice for the decay rate would be to prescribe λ as a user-defined constant, for example based on the value inferred from Fig. 1b. However, such a choice would produce strongly case-dependent behaviour, since the effective decay of the LKE is expected to vary with the ambient turbulence and atmospheric stability. The intended application of the LKE parameterization is to couple it with existing PBL schemes; therefore, λ should instead adapt to the modelled turbulence conditions from the PBL.

A suitable choice for λ is a ratio of dissipation rate to TKE, the reciprocal of what has often been called the *relaxation* time scale τ in canopy studies (Katul et al., 2013; Banerjee et al., 2017):

$$\tau \sim \frac{\langle \bar{k} \rangle}{\langle \bar{\epsilon} \rangle}, \qquad \lambda = \tau^{-1} \sim \frac{\langle \bar{\epsilon} \rangle}{\langle \bar{k} \rangle}. \tag{8}$$

Using a PBL scaling $\langle \bar{\epsilon} \rangle \sim \langle \bar{k} \rangle^{3/2}/\ell$, gives $\lambda \sim \langle \bar{k} \rangle^{1/2}/\ell$, where $\langle \bar{k} \rangle^{1/2}$ and ℓ are the velocity and the length scales (Wyngaard, 2010). In flows within canopies or urban elements, the dissipation parameterization accounts for a length scale related to the obstacle geometry (e.g. Sanz, 2003; Sogachev et al., 2012; Dellwik et al., 2019; Santiago and Martilli, 2010; Nazarian et al., 2020; Lu et al., 2024). By the same analogy, we introduce $D_{0,\mathrm{eff}}$, an "effective" rotor diameter for the grid cell, obtained as the mean rotor diameter of the turbines it contains. This serves as the characteristic length scale for turbine wakes leading to the scaling

$$\lambda \propto \frac{\langle \bar{k} \rangle^{1/2}}{D_{0,\mathrm{eff}}}. \tag{9}$$

To embed this scaling within a given PBL closure, we express it in terms of the scheme's parameters. In 1.5-order PBL closures, the eddy diffusivity for momentum is commonly defined as

$$K_{\mathrm{m}} = \ell \langle \bar{k} \rangle^{1/2} S_{\mathrm{m}}, \tag{10}$$

where ℓ is the mixing length and S_{m} is a stability function or constant. Then, we recast Eq. (9) using K_{m} and ℓ:

$$\lambda = c_\lambda \frac{K_{\mathrm{m}}}{\ell D_{0,\mathrm{eff}}}, \tag{11}$$

where c_λ is introduced as a dimensionless calibration parameter. Expressing λ in terms of K_{m} from the PBL scheme has the advantage that atmospheric stability is implicitly included through the stability function S_{m}. Equation (11) is evaluated locally ($\lambda(x_j, t)$) which provides a dynamical response of the decay rate to the modelled ambient conditions.

2.2.2 Parameterization of the source term

The Q term can be interpreted as the sum of the source terms in Eq. (5): $Q = \langle \bar{\mathcal{P}}_{\mathrm{d}} \rangle + \langle \bar{\mathcal{F}}_{\mathrm{d}} \rangle$. From Fig. 1a, we can neglected the contributions from $\langle \bar{\mathcal{P}}_{\mathrm{d}} \rangle$, leading $\langle \bar{\mathcal{F}}_{\mathrm{d}} \rangle$ as the main source. We compute $\langle \bar{\mathcal{F}}_{\mathrm{d}} \rangle$ following the turbine-induced TKE derivation from Abkar and Porté-Agel (2015), here presented as the LKE source (see Appendix C for details):

$$Q \approx \langle \bar{u}'' \bar{f}'' \rangle = -\langle \bar{f} \rangle \langle \bar{v}_h \rangle a_x. \tag{12}$$

https://doi.org/10.5194/egusphere-2026-2144
Preprint. Discussion started: 22 April 2026

Here, $\langle \bar{f} \rangle$ and $\langle \bar{v}_h \rangle$ represent the grid-cell-averaged force and speed (at hub height h) respectively. The axial induction factor a_x is estimated using the thrust coefficient C_T via 1D momentum theory: $a_x = \frac{1}{2}\left(1 - \sqrt{1 - C_\mathrm{T}}\right)$, where $C_\mathrm{T} < 1$. The force $\langle \bar{f} \rangle$ in Eq. (12) is adopted from V2015 (see Eq. C5), with the initial length scale, σ_0, parameter partially controlling the vertical distribution of the force. We retain a fixed vertical distribution for the LKE source within the rotor area (as in Abkar and Porté-Agel, 2015; Fitch et al., 2012), but also permit the extension of the momentum deficit beyond this area. Consequently, the force, $\langle \bar{f} \rangle$, is computed twice: first modifying the momentum tendencies with a user-defined σ_0, and second for the LKE source, fixing $\sigma_0 = 0.6 r_0$), where r_0 is the rotor radius following GS2024.

2.3 Implementation in the WRF model and compatibility with different PBL schemes

We implement Eq. (7) in the WRF model by treating C as a prognostic scalar. The model dynamics handle the lef-hand side of Eq. (7), while the right-hand side is implemented as a dedicated LKE submodule within the EWP routine.

The variable C is declared as a `scalar` array following the standard WRF configuration for prognostic tracers. This ensures that advection and diffusion are performed automatically by the dynamical core using the same numerical schemes applied to other prognostic scalars such as moisture or passive tracers. The decay term $-\lambda C$ is evaluated in grid cells where C exceeds zero, while the source term Q is limited to cells containing turbines. For the computation of the right-hand side of Eq. (7), we made available the access to several PBL variables, including eddy diffusivity for momentum, turbulent length scale, and either TKE or QKE (twice the TKE).

The conversion from LKE to TKE proceeds in two steps. First, the tendency $(-\lambda C + Q)$ is computed, and λC, which represents the sink of LKE and corresponding source of TKE, is added to the prognosed TKE of the PBL scheme (i.e., $\lambda C = \mathcal{S}_\mathrm{wt}$ in Eq. 3). If the scheme prognoses QKE, the source term is multiplied by two before addition. Then, the dynamical core advects and diffuses C alongside other scalar tracers.

Since the LKE tracer are advected by the WRF dynamical core, advection of TKE by the PBL scheme is not required for the wake contribution; however, if advection of TKE from the PBL scheme (e.g. in MYNN or other newer schemes) is desired, the TKE source is added to the scalar carrying the TKE advection term (e.g. `QKE_ADV` in the MYNN scheme).

3 Model setups and evaluation methods

3.1 Model configurations

We evaluate the results of the LKE model with idealised LES and mesoscale simulations using the same WRF model setup (version 4.2.2) outlined by GS2024. These simulations use a simplified physics configuration, with mesoscale and LES using a surface layer scheme and only the mesoscale setup incorporating a PBL scheme. The study uses two computational domains for mesoscale and LES setups: an outer domain to develop the Atmospheric Boundary Layer (ABL) and a nested domain focused on wind farm modelling. Key configuration parameters (e.g., vertical and horizontal grid spacing), including shared and unique settings for LES and mesoscale setups, are detailed in Table 1.

https://doi.org/10.5194/egusphere-2026-2144
Preprint. Discussion started: 22 April 2026

Table 1. Common and specific configuration settings for the LES and mesoscale simulations using the WRF model.

Common setup for LES and Mesoscale		
Vertical discretization	120 vertical levels with model top at 2 km. First lowest 40 model levels with 5 m of spacing	
Damping layer	Rayleigh damping for the upper 400 m layer	
Horizontal grid	Two domains with a grid aspect ratio of 1:3	
Nesting	One-way nesting	
Lateral boundary conditions	Periodic for the outer domain and nested for the inner domain	
Surface roughness length	2×10^{-4} m (offshore conditions)	
Coriolis parameter	1.2×10^{-4} s^{-1}	
Specific setup	**LES**	**Mesoscale**
Horizontal grid points (n_x, n_y)	D1 = [700,500], D2 = [1200,700]	D1 = [108,96], D2 = [289,97]
Horizontal discretization [m] $(\Delta x = \Delta y)$	D1 = 60, D2 = 20	D1 = 3600, D2 = 1200
Model time step [s] (Δt)	D1 = 1.5, D2 = 0.5	D1 = 24, D2 = 8
Spin-up time [h]	8	120
Total run time [h]	12	130
Output frequency [s]	10	600

D1 = Outer domain, D2 = Nested domain

For the LES setup, we adopt the TKE-based sub-grid scale (SGS) model by Deardorff (1980) for the parameterization of momentum and heat SGS fluxes. In the mesoscale setup, we use three local 1.5-order PBL schemes to simulate turbulence processes in the vertical: the MYNN, the Mellor-Yamada Janjic (MYJ; Janjić, 1990), and the Bougeault and Lacarrere (BouLac; Bougeault and Lacarrere, 1989) schemes. The mesoscale setups employing MYNN and BouLac, as well as the LES setups, utilise the Revised Monin-Obukhov scheme (Jiménez et al., 2012) for the surface layer (option `sf_sfclay_physics = 1`), while the MYJ scheme employs its modified Monin-Obukhov scheme (option `sf_sfclay_physics = 2`; Janjić, 2001).

All simulations start with a dry, neutral ABL featuring a uniform geostrophic wind and a potential temperature profile set at 290 K up to 700 m. Above this height, the potential temperature increases at a rate of 10 K km^{-1}. Mesoscale simulations include a capping inversion layer above the inversion height with a 0.02 K m^{-1} gradient and a 100-meter thickness to limit boundary layer growth. Each LES and mesoscale simulation, and in the three PBL schemes, starts with a tailored geostrophic wind to archive a mean wind speed of 10 m s^{-1} and mean wind direction of 270° at 119 m height at the last hour of the simulations.

Initially, the LES and mesoscale simulations are run only for the outer domain to establish a steady neutral ABL (see spin-up time in Table 1). After achieving a steady-state solution, we add the nested domain for an additional 10 hours for mesoscale and two hours for LES. Subsequently, simulations restart at the spin-up time to model the wind farm within the nested domains

https://doi.org/10.5194/egusphere-2026-2144
Preprint. Discussion started: 22 April 2026

for these additional hours. Table 1 outlines the total simulation times and spin-up requirements for both LES and mesoscale simulations.

3.2 Wind farm modelling

The modelled wind farm consists of a 6×6 array of DTU 10-MW reference turbines (Bak et al., 2013), each with a 119-meter hub height and a 178.3-meter rotor diameter, which aligns with the model's x-y directions, as illustrated in Fig. 2 for the LES's nested domain. Turbines are spaced 6.7 rotor diameters (D_0) apart, matching the mesoscale grid spacing (1.2 km). This configuration ensures each turbine's central placement within its mesoscale grid cell to mitigate sub-grid scale wake interactions.

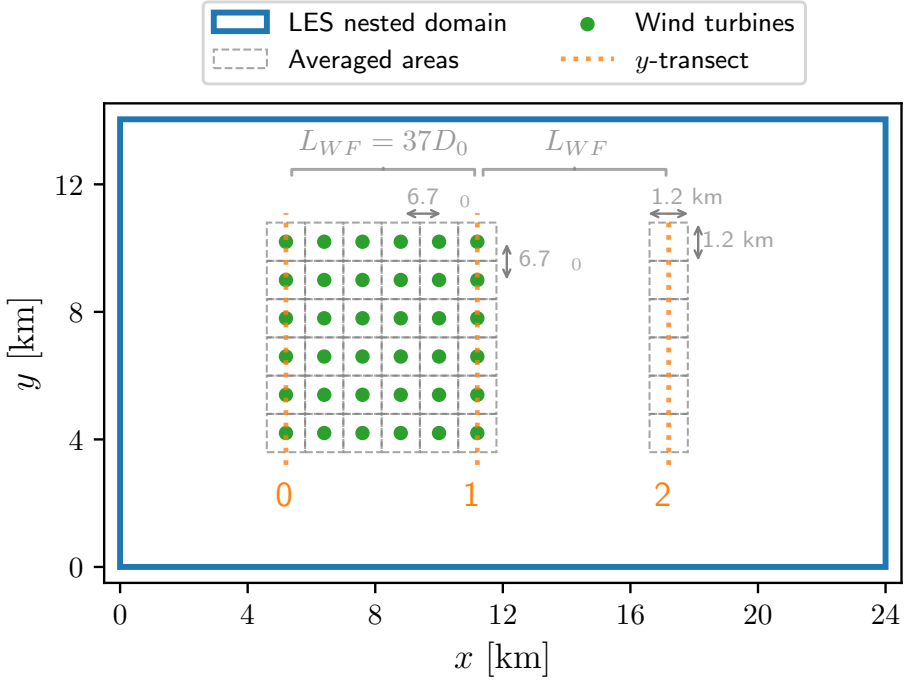

Figure 2. Representation of the modelled wind farm in the LES nested domain. The y-transects serve as a reference for the evaluation and are sequentially spaced by a wind farm length (L_{WF}) apart. Labels 0, 1, and 2 in transects, represent the front row, last row, and one L_{WF} distance past the last row, respectively. D_0 is the rotor diameter, while dashed grey squares exemplify the mesoscale grid cells and the average areas used to post-process the LES results.

We implement the actuator disc (AD) model from Mirocha et al. (2014), incorporating tip correction factors from Shen et al. (2005) and validated by Peña et al. (2022), to simulate wind farm effects on flow within the LES nested domain. Within the mesoscale's nested domains, we model turbine impacts through three wind farm parameterizations: the original EWP (V2015), the Fitch parameterization (Fitch et al., 2012), and our newly developed LKE model integrated in the EWP (see Sect. 2).

https://doi.org/10.5194/egusphere-2026-2144
Preprint. Discussion started: 22 April 2026

For the original EWP, we use $\sigma_0 = 1.7\,r_0$ (recommended by V2015). In the Fitch parameterization, we adopt a $c_f = 0.25$ (Archer et al., 2020) and explore using $c_f = 0.$ (representing no TKE generation) and $c_f = 1$. The parameter c_f denotes a fraction of the total TKE source term in the Fitch parameterization (Archer et al., 2020). These parameter values are applied across all PBL schemes.

For the LKE model, we investigate the impact of varying the coefficient c_λ from 0.0 to 1.0, only using the MYNN scheme (TKE advection deactivated) and setting $\sigma_0 = 0.6\,r_0$. We also conduct tests using a consistent $c_\lambda = 0.4$ (from Sect. 2.2.1) with $\sigma_0 = 0.6\,r_0$, and $1.2\,r_0$. Furthermore, we adjust σ_0 and c_λ for each PBL scheme. Table 2 provides a detailed comparison of wind farm simulations using the three parameterizations, highlighting the specific parameters chosen for each PBL scheme and test.

3.3 Evaluation methods

We time-average the results from the LES and mesoscale nested domains over the last hour of the simulation (see total run times in Table 1). Following an analogous approach as in GS2024, we further average the time-mean LES results across 1.2 km by 1.2 km areas centred on turbines, as illustrated in Fig. 2.

Our study evaluates the TKE modelled by the LKE model by comparing it with other wind farm parameterizations (EWP and Fitch) and using LES with actuator discs (LES-AD) as the reference. We calculate the total TKE from the LES results, adding the SGS contributions to the resolved TKE obtained from 10-second outputs of the final hour of the simulation. We also examine the impact of the wind farm-added TKE on the wind speed recovery and the added TKE under various PBL schemes.

To compare the models, we examine the vertical profiles and cross-sectional fields from the averaged LES and mesoscale results, focussing on the front row, exit row, and one wind farm length (L_{WF}) past the last row (y-transects 0, 1 and 2 in Fig. 2). We present these profiles and fields as the differences between simulations with minus without the wind farm. Additionally, we introduce the normalised difference in turbulent kinetic energy (NDTKE), calculated throughout the domain and vertically integrated from the surface up to $2D_0$ =356.6 m:

$$\mathrm{NDTKE} = \frac{\int_0^{2D_0} \langle \bar{k}^{\eta}_{\mathrm{WF}} \rangle \, dz - \int_0^{2D_0} \langle \bar{k}^{\eta}_{0} \rangle \, dz}{L_{\mathrm{WF}}^{-2} \int_0^{L_{\mathrm{WF}}} \int_0^{L_{\mathrm{WF}}} \int_0^{2D_0} \langle \bar{k}_{0,\mathrm{ref}} \rangle \, dz \, dx \, dy} \tag{13}$$

Here, $\bar{k}_{\mathrm{WF}}$ and $\bar{k}_0$ represent the TKE from each specific simulation η, in scenarios with and without the wind farm, respectively. To account for inflow TKE variability across different PBL schemes and LES, as discussed in Appendix B, we normalise all differences using the LES inflow TKE ($\bar{k}_{0,\mathrm{ref}}$) averaged over the wind farm area. Lastly, to focus on streamwise variations, we average the NDTKE and the wind speed deficit in the y-direction as delimited by the y-transects in Fig. 2.

https://doi.org/10.5194/egusphere-2026-2144
Preprint. Discussion started: 22 April 2026

Table 2. Overview of the wind farm simulations and their labels. Refer to the main text for details and definitions of parameters.

Mode	PBL	PBL's TKE advection	Model	Parameter values	Label
Mesoscale	MYNN	on	Fitch	$c_f = 0.0$	Fitch-shear-adv
				$c_f = 0.25$ (default)	Fitch-ctrl-adv
				$c_f = 1.0$ (original)	Fitch-100-adv
			EWP	$\sigma_0 = 1.7\,r_0$ (default)	EWP-ctrl-adv
			EWP+LKE	$\sigma_0 = 0.6\,r_0$, $c_\lambda = 0.4$	LKE-ctrl-adv
		off	Fitch	$c_f = 0.0$	Fitch-shear
				$c_f = 0.25$ (default)	Fitch-ctrl
			EWP	$\sigma_0 = 1.7\,r_0$ (default)	EWP-ctrl
			EWP+LKE	$\sigma_0 = 0.6\,r_0$, $c_\lambda = 0.0$	LKE-shear
				$\sigma_0 = 0.6\,r_0$, $c_\lambda = 0.4$	LKE-ctrl
				$\sigma_0 = 1.2\,r_0$, $c_\lambda = 0.4$	LKE-opt
				$\sigma_0 = 0.6\,r_0$, $c_\lambda = \{0.0, \ldots, 1.0\}$	LKE-range
	MYJ	off (option not available)	Fitch	$c_f = 0.0$	MYJ-Fitch-shear
				$c_f = 0.25$	MYJ-Fitch-ctrl
			EWP+LKE	$\sigma_0 = 1.0\,r_0$, $c_\lambda = 0.4$	MYJ-LKE-opt
	BouLac	off (option not available)	Fitch	$c_f = 0.0$	BL-Fitch-shear
				$c_f = 0.25$	BL-Fitch-ctrl
			EWP+LKE	$\sigma_0 = 0.6\,r_0$, $c_\lambda = 0.4$	BL-LKE-opt
LES	-	-	AD	-	LES-AD-hres (original resolution) LES-AD (spatially averaged)

https://doi.org/10.5194/egusphere-2026-2144
Preprint. Discussion started: 22 April 2026

4 Comparison of LKE with conventional parameterizations

4.1 Spatial analysis of TKE differences

Our evaluation starts with a spatial comparison of the wind farm's added TKE, contrasting the LKE model with the Fitch parameterization and using LES-AD as the benchmark. Figure 3 illustrates the TKE differences at hub height between the simulations with minus the one without the wind farm. In Fig. 3a, we show the LES results at the original resolution (LES-AD-hres), where the square wind farm configuration (Fig. 2) results in turbines being fully impacted by the wakes of upstream ones. At this granularity, downstream turbines experience TKE increases of more than 1.0 $m^2\ s^{-2}$, surpassing the values of other simulations discussed in this section. For comparison with wind farm parameterizations, we average the LES-AD-hres TKE to the mesoscale resolution as shown in Fig. 3b—hereafter denoted simply as LES-AD. In this spatially-averaged LES results, the first row appears similar to the ambient TKE due to averaging effects, with subsequent rows showing a streamwise increase in TKE, peaking at 0.6 $m^2\ s^{-2}$ at the farm's last row before gradually decreasing.

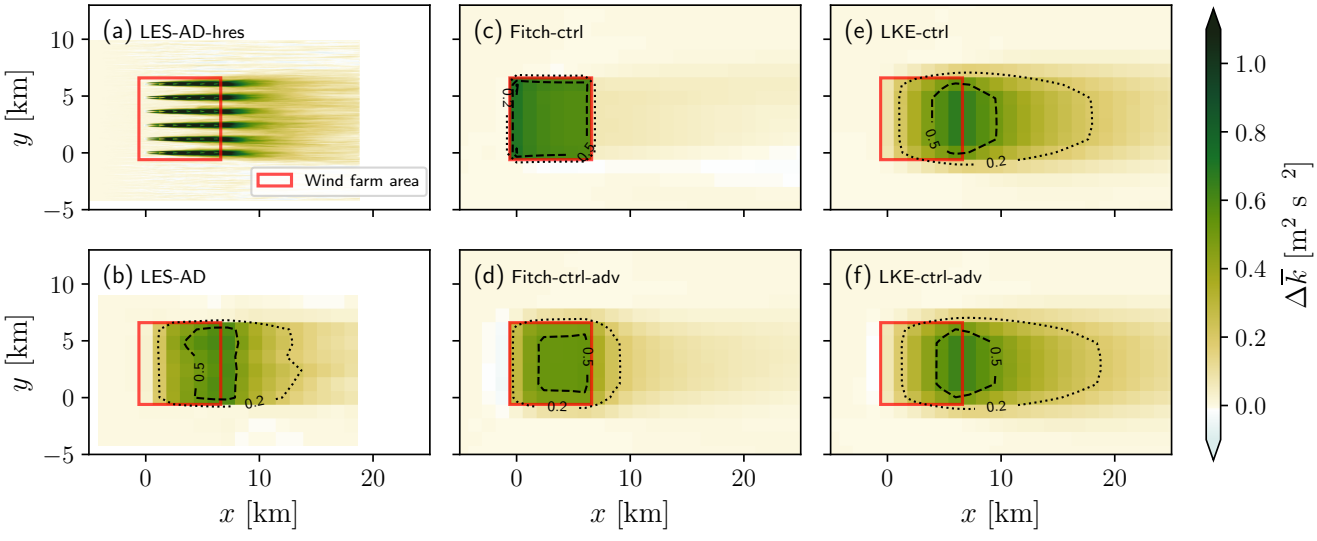

Figure 3. Time-averaged TKE differences (between simulations with and without the wind farm) at hub height using as reference (a) LES-AD-hres and (b) LES-AD and comparing (c) Fitch-ctrl, (d) Fitch-ctrl-adv, (e) LKE-ctrl, and (f) LKE-ctrl-adv. Suffix "-adv" indicate TKE advection activated from the MYNN scheme. See Table 2 for details and parameter values.

The Fitch parameterization yield different results based on whether TKE advection is enabled. As expected, without TKE advection, Fitch's approach (Fitch-ctrl; Fig. 3c) restricts TKE increases to cell-containing turbines, showing nearly uniform differences ($\approx 0.5\ m^2\ s^{-2}$) across the farm. Activating TKE advection enhances Fitch's performance (Fig. 3d), mirroring the increasing TKE trend of the LES-AD towards the farm's end. However, the magnitude of the difference in TKE in the Fitch-

https://doi.org/10.5194/egusphere-2026-2144
Preprint. Discussion started: 22 April 2026

ctrl-adv simulation is smaller than that of the LES-AD. Note that the Fitch-ctrl-adv simulation also introduces a TKE reduction upstream of the wind farm front row that is not present in the LES-AD reference.

In contrast to simulations using the Fitch scheme, the LKE model captures both the LES-AD trend and magnitude of TKE, with a minimum at the front row, a peak at the last row, and a subsequent decay downstream, regardless of the MYNN TKE advection setting (Fig. 3e–f). The LKE model predicts a slightly larger spatial extent of the added TKE than the reference: for example, the 0.2 $m^2\,s^{-2}$ contour in Fig. 3 extends downstream to approximately 18 km, whereas in LES-AD it reaches only about 14 km.

4.2 Comparison of added TKE

To streamline the comparison of TKE changes across our simulations, we focus on the normalised difference in TKE (NDTKE; Eq. 13). Figure 4 aggregates the streamwise variation of NDTKE from LES-AD, Fitch-ctrl, and LKE-ctrl, including additional simulations: the original EWP (EWP-ctrl) and the Fitch parameterization without TKE injection (Fitch-shear). These two last additions rely on the resolved shear, derived from the momentum sink, for TKE generation. As described in Sect. 3.3, all parameterizations and LES-AD simulations are normalised using the LES inflow TKE, meaning that a value of 1.0 shown in Fig. 4 indicates a 100 % increase over that reference TKE.

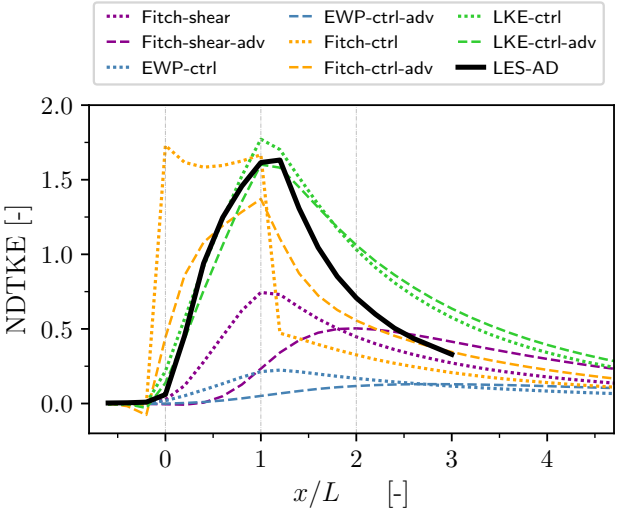

Figure 4. Comparison of the streamwise NDTKE (Eq. 13) using different parameterizations: Fitch with TKE injection (Fitch-ctrl) and only shear contributions (Fitch-shear), LKE (LKE-ctrl) and the original EWP (EWP-ctrl), with LES-AD as the baseline. The impact of TKE advection enabled (dashed lines; suffix "-adv") and disabled (dotted lines) is shown. Vertical grey lines indicate the location of the y-transects referenced in Fig. 2, and Table 2 provides the simulation's details.

The LES-AD simulation in Fig. 4 reiterates previous details in Fig. 3: minimal added TKE at the front row, peaking at the farm's end, and gradually decreasing downstream. The Fitch-ctrl simulation highlights a significant accumulation of TKE

https://doi.org/10.5194/egusphere-2026-2144
Preprint. Discussion started: 22 April 2026

within the wind farm area, particularly in the front row (150 % of the reference TKE), followed by a sharp decrease after the last row. Introducing TKE advection (Fitch-ctrl-adv) redistributes TKE downstream, reducing the maximum TKE at the last row by 30 %, but with a better streamwise distribution of TKE.

For simulations generating TKE solely through resolved shear and without MYNN's TKE advection (Fitch-shear and EWP-ctrl), their streamwise distribution of NDTKE follows that of the LES-AD but with a much smaller magnitude. The key difference between the Fitch-shear and EWP-ctrl runs (the former with more TKE than the latter) lies in the vertical distribution of the momentum sink, with the Fitch-shear simulation concentrating it within the rotor area and the EWP-ctrl extending it beyond. A concentrated momentum sink produces a larger gradient of wind speed in the vertical; thus, more shear-generated TKE than the distributed momentum sink. Activating TKE advection in those simulations shifts the streamwise TKE downstream and further reduces their TKE peak. The latter suggests that if an explicit source is not included in the wind farm parameterizations, it is better to deactivate the advection of TKE from the MYNN scheme.

The LKE model performs similarly regardless of the state of the MYNN TKE advection (see Sect. 2.3). However, consistent with the spatial analysis, the LKE simulations exhibit higher TKE levels than the reference downstream of the wind farm. Despite this overestimation, the model reproduces the overall shape of the streamwise evolution of the added TKE observed in the LES-AD reference. The following section investigates the origin of this overestimation and examines the factors modulating the total TKE, with particular emphasis on the interplay between the PBL scheme and the LKE model formulation.

5 Factors determining the wind farm-added TKE in the LKE model

5.1 The effects of the new parameter c_λ on TKE and wind speed

In Sect. 2.2.1, we introduced the parameter c_λ in Eq. (11), that partially adjust the rate at which LKE decays into TKE in the LKE model. We investigate the impact of manipulating c_λ (LKE-range simulations in Table 2) on NDTKE (Fig. 5a), and the subsequent wake recovery (Fig. 5b) at hub height, using the same inflow wind speed ($\bar{v}_0 = 10\,\mathrm{m\,s^{-1}}$) and the same momentum sink distribution ($\sigma_0 = 0.6\,r_0$) in all cases. For comparison, two Fitch simulations are included in Fig. 5 denoting the rage ([0,1]) of the TKE coefficient in the parameterization (Fitch-shear and Fitch-100-adv respectively; see Table 2 for details).

The LES-AD simulation exhibits a 160 % increase in added TKE and a 10 % reduction in wind speed at the end of the wind farm. Sensitivity tests with c_λ values ranging from 0 to 1 show that the added TKE increases from approximately 60 % to 250 %, accompanied by a reduction in wind speed deficit from 17.5 % to 12.5 % in the last row of the farm. The Fitch parameterization produces a larger range of added TKE than the LKE model. However, using 100 % of the TKE source in the Fitch approach (corresponding to a 350 % increase in TKE) results in a wind speed reduction of 12.5 %, comparable to the LKE simulation with $c_\lambda = 1$. This indicates that, with the Fitch parameterization, more than 3.5 times the reference TKE must be injected for the wind speed deficit to approach that of the LES-AD reference.

The tested c_λ values in Fig. 5 lead to distinct streamwise evolutions of the added TKE. The most pronounced differences occur in the magnitude of the peak at the farm's end ($x/L_{WF} = 1$ in Fig. 5a) and in the downstream distribution of the TKE addition. Larger c_λ values lead to a faster conversion of LKE to TKE, resulting in a more rapid depletion of the LKE source and

https://doi.org/10.5194/egusphere-2026-2144
Preprint. Discussion started: 22 April 2026

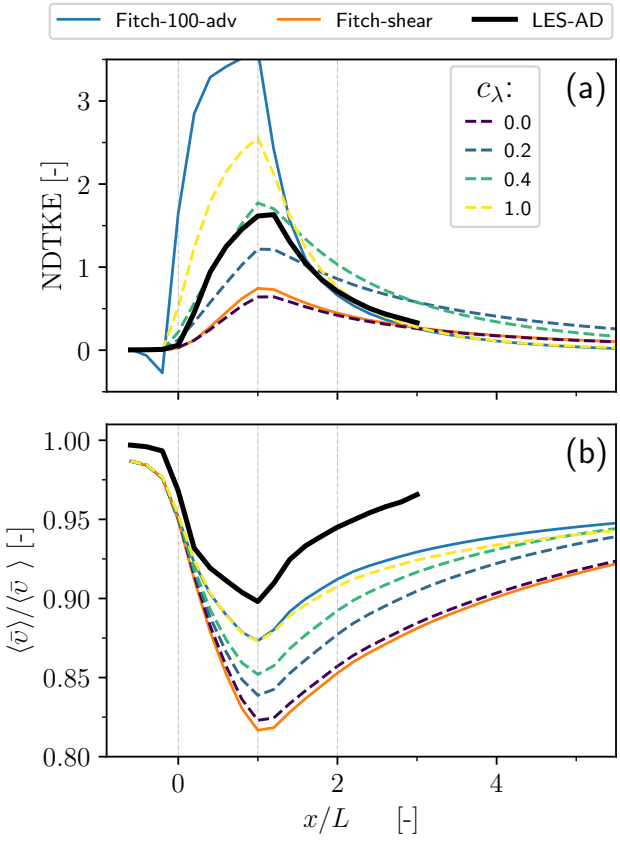

Figure 5. Effect of varying c_λ values on the (a) NDTKE and the (b) hub-height wind speed deficit in the LKE-range simulations with a constant momentum sink distribution ($\sigma_0 = 0.6\,r_0$). The LES-AD, Fitch-100-adv and Fitch-shear results are shown as a reference (see Table 2 for details). Vertical grey lines indicate y-transects referenced in Fig. 2.

a faster accumulation of TKE within the wind farm. In contrast, smaller c_λ values delay the conversion process and the release of TKE. For instance, $c_\lambda = 0.2$ yields TKE levels below the LES-AD reference within the wind farm, while producing higher TKE downstream of the farm ($x/L_{WF} \geq 1$). When $c_\lambda = 0$, the model reverts to its original formulation (i.e. EWP without a TKE source but with $\sigma_0 = 0.6 r_0$), yielding TKE additions and wind speed deficits comparable to those obtained with the Fitch parameterization without a TKE source (Fitch-shear in Fig. 5). These two configurations produce the deepest wind wakes among the tested cases, nearly doubling the wind speed deficit relative to the LES-AD reference at the farm's end (Fig. 5b).

Regarding wind wake recovery (Fig. 5b), all c_λ values exhibit a similar recovery trend up to approximately one wind-farm length downstream of the last row ($1 \leq x/L_{WF} \leq 2$), with different magnitudes of wind speed deficit. Farther downstream, the recovery rates diverge, with higher c_λ values associated with slower recovery.

A noteworthy detail is the considerable reduction in wind speed of approximately 2.5 % at hub-height 1.2 km upstream of the first turbine row in all mesoscale simulations, contrasting with a reduction of approximately 0.6 % in the LES-AD at that

https://doi.org/10.5194/egusphere-2026-2144
Preprint. Discussion started: 22 April 2026

point. At the first row of turbines, the magnitude of the reduction in the mesoscale simulations is ∼5 %, irrespective of the value of c_λ, compared to a decrease of only 2.5 % in the LES-AD simulations. In the mesoscale simulations, this upstream reduction can be attributed in part to WRF's numerical diffusivity, with a fraction potentially attributable to resolving some large-scale blockage.

Based on the sensitivity analysis shown in Fig. 5a, an intermediate value of c_λ provides the best agreement with the LES-AD reference in terms of TKE addition within the wind farm. However, the corresponding wind speed deficit still underestimates the reference, yielding a reduction of approximately 15 % at the farm's end. In the LKE framework (as in the EWP), this discrepancy can be further addressed by adjusting the parameter σ_0, allowing the wind speed deficit to be tuned independently of the TKE addition.

5.2 TKE changes via shear production

The other factor controlling the amount of TKE added by the turbines is the shear production parameterized within the PBL scheme. As introduced earlier, variations in this shear-generated TKE are achieved by modifying the vertical distribution of the momentum sink (see *EWP-ctrl* and *Fitch-shear* in Fig. 4). Here, we examine how different levels of shear-generated TKE, obtained by varying the parameter σ_0, interact with the explicit TKE source introduced by the LKE model. This interaction is analysed through three LKE simulations, all evaluated against the LES-AD reference. The first case employs a momentum sink concentrated within the rotor area without an explicit TKE source (LKE-shear; $\sigma_0 = 0.6\,r_0$, $c_\lambda = 0.0$). The second case applies the same momentum sink while activating the TKE source (LKE-ctrl; $\sigma_0 = 0.6\,r_0$, $c_\lambda = 0.4$). The third case combines a vertically extended momentum sink beyond the rotor region with consistent TKE addition (LKE-opt; $\sigma_0 = 1.2\,r_0$, $c_\lambda = 0.4$). The value $\sigma_0 = 0.6\,r_0$ is chosen to emulate the Fitch-shear configuration, following GS2024.

Figure 6 presents the vertical profiles of differences between simulations with and without wind farms for the wind speed and TKE of the mentioned cases at the farm's end (y-transect 1 in Fig. 2). The figure also includes the differences for the shear ($\langle\bar{\mathcal{P}}_\mathrm{s}\rangle$) and wake production ($\langle\bar{\mathcal{P}}_\mathrm{w}\rangle$) terms derived from the TKE budget outputs from the MYNN PBL scheme. From the three simulation cases, the LKE-shear has the most pronounced reduction of wind speed in the rotor area (almost twice the reference at hub height) but the least above it (Fig. 6a). The LKE-shear profile of $\Delta\langle\bar{k}\rangle$ indicates lower TKE production, from $1.8\,D_0$ down to the surface, compared to the LES-AD, and shows a TKE "sink" near the ground absent in the reference (Fig. 6b). However, it captures the TKE peak's location as seen by the LES-AD reference, which can also be observed by the maximum value of the shear production term located at the upper rotor tip (Fig. 6c).

Incorporating TKE via $c_\lambda = 0.4$ in the model results in greater TKE (LKE-ctrl in Fig. 6b) than the LKE-shear and LES-AD, reducing the $\Delta\langle\bar{v}\rangle$ profile through increased mixing. Despite this additional mixing, the wind speed profile of the LKE-ctrl remains higher (in absolute magnitude) than the LES-AD (Fig. 6a). Exploration of c_λ sensitivity (Fig. 5) suggests that a $c_\lambda > 1.0$ might align the hub-height wind deficit with the LES-AD but at the cost of excessive (referring to the LES baseline) TKE increase. An alternative solution can be adjusting $\sigma_0 = 1.2\,r_0$ while maintaining $c_\lambda = 0.4$, which leads to the LKE-opt scenario. Increasing σ_0 smooths the $\Delta\langle\bar{v}\rangle$ profile, which in turn reduces the TKE addition from shear production (weaker

https://doi.org/10.5194/egusphere-2026-2144
Preprint. Discussion started: 22 April 2026

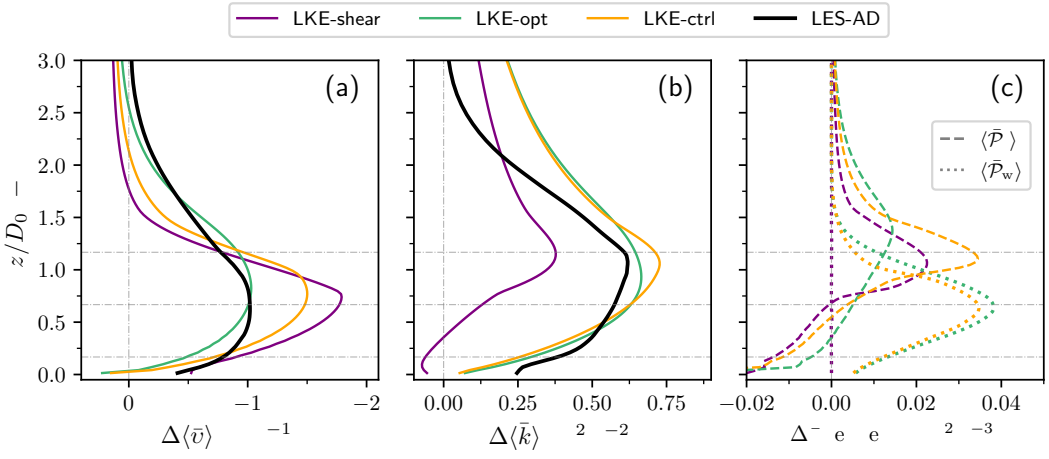

Figure 6. Vertical profiles at the last turbine row (y-transect 1 in Fig. 2) showing differences (simulations without minus with wind farms) in (a) wind speed, (b) TKE, and (c) Twice TKE production ($\langle\bar{q}\rangle$) by shear ($\langle\mathcal{P}_s\rangle$; dashed lines) and wake ($\langle\mathcal{P}_w\rangle$; dotted lines) for LKE-shear, LKE-ctrl and LKE-opt simulations (refer to Table 2 for details). Wind speed and TKE results from the LES-AD simulations are included for reference. Horizontal grey lines mark the rotor's top, bottom, and hub heights.

vertical gradient of wind speed than in the other two cases). This combination of parameters closely aligns the wind speed and TKE profiles to the one from the LES-AD.

Assessing the shear and wake production terms in Fig. 6c offers insights into their variations across the LKE cases. Although similar shear production is expected between LKE-shear and LKE-ctrl due to identical σ_0 values, adding TKE in LKE-ctrl increases shear production. This effect is attributed to enhanced eddy diffusivity (from the additional TKE that comes from the explicit source) used in the parameterization of the Reynolds stresses. With the same c_λ, the LKE-ctrl and LKE-opt simulations exhibit similar wake production, with a slight increase at hub height for LKE-opt, attributed to higher hub-height wind speed due to the distributed momentum sink and mixing. The differences in shear production between the LKE-ctrl and LKE-opt simulations arise from their respective momentum sink distributions—reducing σ_0 increases shear production and vice versa. The latter highlights how σ_0 directly modifies the wind speed profiles and indirectly modulates TKE generation by influencing shear production, particularly near the upper rotor tip.

6 Assessing the LKE model across different PBL schemes

We test the LKE model with the BouLac and MYJ PBL schemes and compare their performance against the Fitch parameterization and the LES-AD reference. This comparison extends our previous examination (Sect. 4) of the Fitch and LKE models using the MYNN PBL scheme, maintaining identical parameters for both models using the MYJ and BouLac schemes.

Figure 7 presents the streamwise comparison of the NDTKE and hub-height wind speed deficit for the Fitch-ctrl, Fitch-shear, and LKE-opt simulations using the MYJ and BouLac PBL schemes (see Table 2). LKE-opt simulations have adjusted values

https://doi.org/10.5194/egusphere-2026-2144
Preprint. Discussion started: 22 April 2026

of σ_0 for each PBL scheme. The Fitch-ctrl's TKE pattern using both PBL schemes (Fig. 7a) mirrors its behaviour using the MYNN scheme without TKE advection (Fig. 4): limited added TKE to the turbine-containing cells. In contrast, the LKE-opt simulations using the MYJ and BouLac schemes (hereafter MYJ-LKE-opt and BL-LKE-opt; Fig. 7) reproduce the streamwise TKE evolution observed in the LES-AD reference. In particular, the BL-LKE-opt case closely matches the LES-AD in terms of added TKE magnitude, whereas the MYJ-LKE-opt simulation produces approximately 60 % less added TKE at the last row of the wind farm compared to LES-AD.

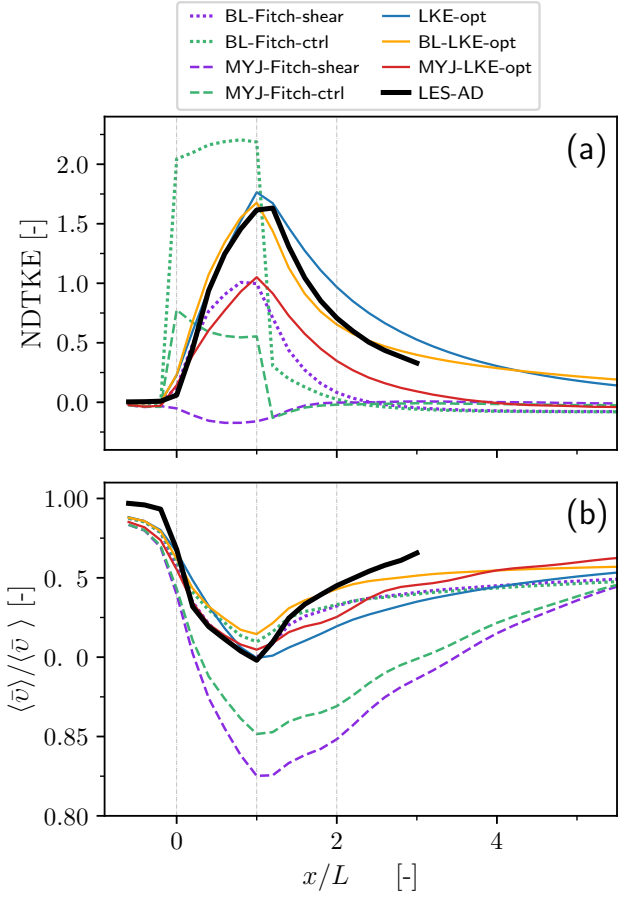

Figure 7. Similar to Fig. 5, but for the LKE and Fitch parameterizations using the MYJ (dashed lines) and BouLac ("BL" dotted lines) PBL schemes. Refer to Table 2 for details of each simulation.

The added TKE in the simulations varies significantly under the different PBL schemes despite identical wind farm parameterization settings, with the simulations using BouLac scheme generally producing higher TKE levels than those using MYJ. These differences are evident in the Fitch-shear simulations (no explicit TKE source) with these PBLs. Under the BouLac PBL scheme, Fitch-shear (Fig. 7a) generates TKE of comparable magnitude to the Fitch-ctrl case with an explicit source using the

https://doi.org/10.5194/egusphere-2026-2144
Preprint. Discussion started: 22 April 2026

MYNN scheme (Fig. 4), but still is 60 % less than the LES-AD at the farm's end. Surprisingly, Fitch-shear under MYJ results in a TKE sink within the wind farm area, which then recovers to ambient levels three farm lengths downstream (Fig. 7a). While the cause of this behaviour is beyond the scope of the present study, it highlights the importance of including an explicit TKE source when using the MYJ scheme. Moreover, it suggests that a large TKE source may be required to approach LES-AD TKE levels, as this PBL scheme appears to contribute little TKE through shear production.

The comparison of the wind speed deficits in Fig. 7b reveals that MYJ simulations exhibit similar deficits when using the MYNN—greater deficits than those observed in LES-AD. In contrast, BouLac simulations replicate the deficit patterns of the LES-AD more closely in the wind farm area. However, the BouLac simulations also indicate a slower wind speed recovery downstream of the wind farm, diverging from LES-AD at the far wake $x/L_{WF} > 2$ in Fig. 7b. Wind speed deficit patterns in the Fitch simulations under MYJ resemble those of MYNN, without TKE advection (Fig. 4), but with different TKE levels.

Except when using the MYJ scheme, the LKE simulations show differences of less than 10 % in added TKE and less than 2 % in wind speed deficit within the wind farm region ($0 \leq x/L_{WF} \leq 1$). Downstream of the wind farm ($x/L_{WF} \geq 1$), the LKE-opt simulation using MYNN produces approximately 20 % more added TKE than the LES-AD reference, whereas the LKE-opt with the MYJ yields approximately 25 % less. In contrast, the LKE simulation employing the BouLac scheme shows closer agreement with the reference in the downstream region. Overall, wind speed recovery in the LKE simulations aligns more closely with the LES-AD than the Fitch simulations, with the MYJ-based LKE simulation exhibiting the closest match, differing by approximately 2 % downstream.

The LKE-opt runs have a consistent $c_\lambda = 0.4$ and adjusted σ_0 values for the three PBL schemes. This adjustment is to match the LES-AD in terms of wind speed deficit and added TKE. We determine $\sigma_0 = 0.6\,r_0, 1.0\,r_0,$ and $1.2\,r_0$ as the optimal values for the BouLac, MYJ, and MYNN PBL schemes, respectively. Notice that the chosen σ_0 values correspond inversely to the eddy diffusivity values of the PBL schemes: BouLac and MYNN schemes with the largest and smallest values throughout the ABL, respectively (see Appendix B). This adjustment highlights that the magnitude of added TKE, accurately captured by the LKE model in shape, is not the sole determinant in obtaining an accurate wind speed shape. At the same time, this added TKE necessitates consideration of the resolved shear and the specific treatment of TKE by the PBL scheme.

7 Discussion

To ensure an accurate evaluation of the TKE generated by wind farm parameterizations, we chose a LES modelling set-up with an actuator disc as our reference benchmark, circumventing the complexities involved in validating TKE from these parameterizations against actual measurements. In this process, we ensured comparable inflow conditions between the LES and mesoscale simulations, as detailed in Appendix B. The focus thus shifted to ensuring an accurate representation of the turbulence structures in the resolved TKE of the LES. Although increasing LES resolution and implementing advanced turbine representations could enhance turbulence representation, the high computational demand makes this impractical for refining coarser parameterizations. We consider that a 20-meter horizontal resolution in our LES was adequate to evaluate TKE from wind farm parameterizations, showing less than a 2.2 % difference in resolved TKE compared to the 10-meter resolution setup

https://doi.org/10.5194/egusphere-2026-2144
Preprint. Discussion started: 22 April 2026

by GS2024 (see Appendix D). This result supports the validity of our comparative analysis. However, it remains essential to validate these results with field measurements, once they become available, as the application of the wind farm parameterizations is done mainly under realistic scenarios.

The differences in TKE outcomes between LKE and Fitch parameterization lie in their methods of TKE injection and their definitions within the grid-cell-averaged TKE budget equation. The Fitch parameterization incorporates both ensemble and spatial perturbations in its velocity perturbation definition, making the turbine-induced term $\mathcal{P}_\mathrm{f}$ the primary contributor to the added TKE. This leads to immediate injection of TKE at the turbine location, which requires advection of TKE from the PBL to transport TKE further downwind in an attempt to achieve satisfactory results away from the turbine locations, as indicated by previous studies. In contrast, the LKE model focuses on spatial perturbations, with the wake production term predominantly contributing to the added TKE. As explained in Sect. 2, this results in a gradual and measured release of TKE, transitioning from LKE to TKE in a manner that more accurately mirrors the reference LES-AD behaviour (and possibly the real world). Additionally, the added TKE in the LKE parameterization is not merely generated at the turbine's location for subsequent advection, as in the Fitch parameterization, but is produced along the turbine's wake. This is achieved using tracers that provide a "memory" of the turbulence's evolution, leading to a better TKE representation downstream.

The LKE source term (Eq. 12) is inspired by the TKE source term derivation from Abkar and Porté-Agel (2015), which uses a relationship between axial induction and thrust coefficient to model spatial differences. Alternatively, one could adopt the approach of Fitch et al. (2012), which considers the difference between thrust and power coefficients for the LKE source. Although both methods yield similar results in terms of TKE addition, as noted by Ali et al. (2023) in their realistic simulations, preliminary tests indicate a slight increase in TKE at the downstream end of the studied wind farm using Fitch's method compared to Abkar's (not shown). We opted for Abkar's methodology but chose not to include the ζ parameter, which accounts for the discrepancy between the inflow wind speed at the turbine's location ($\bar{u}_{0,wt}$) and the average wind speed across a grid cell ($\langle \bar{u}_0 \rangle$). An interesting possible improvement should account for sub-grid wake interactions (as in the MAV parameterization; Ma et al., 2022), providing a more precise estimation of the inflow wind speed than the standard averaged-grid-cell speed approach. Therefore, in this initial evaluation, we use an ideal wind farm layout where each turbine is located at the centre of the cell to minimise sub-grid effects.

The proposed parameterization of λ, defined as the inverse of a characteristic time scale τ, is intended to account for differences among PBL schemes, including their background TKE levels and closure constants, as well as the characteristic length scale of the drag-inducing elements. The dimensionless coefficient c_λ provides an overall calibration of this conversion. Through λ, the LKE-to-TKE conversion acts as a complementary TKE source that varies according to each scheme's shear production. For example, because the BouLac scheme exhibits larger shear production, it requires a smaller explicit TKE contribution than MYJ to achieve comparable agreement with LES reference. For the three PBL schemes considered here, this formulation effectively narrows the calibration to a common value of $c_\lambda = 0.4$. Although alternative parameterizations of λ could be formulated based on other definitions of characteristic velocity and length scales, the present form (Eq. 11) is direct and practical; further investigation of alternative formulations remains the subject of ongoing work.

https://doi.org/10.5194/egusphere-2026-2144
Preprint. Discussion started: 22 April 2026

The added TKE influences vertical momentum diffusion through the eddy diffusivity and, consequently, wind speed recovery, as shown in the results section. However, as illustrated by the Fitch scheme, introducing an excessively large TKE source within the wind farm area is still insufficient to reproduce the deficit predicted by LES-AD in that region. Matching the LES-AD wind speed therefore requires not only a suitable representation of the added TKE within the wind farm parameterization, but also a mechanism to account for enhanced wake recovery. The LKE model addresses both aspects by using the initial length scale (σ_0, from the EWP) to distribute the momentum sink vertically, while λ modulates the magnitude and structure of the added turbulence. This vertical distribution of the force indirectly accounts for wake recovery by producing a smeared, grid-cell-averaged deficit profile (V2015). An alternative approach would be to include a parameterization of the stress divergence, the primary driver of wake recovery (van der Laan et al., 2023); exploring such an extension is left for future studies.

Including eddy diffusivity in λ implicitly incorporates atmospheric stability into the LKE-to-TKE conversion through the PBL scheme. However, the present analysis is limited to neutral conditions, and further evaluation under stable and unstable regimes is needed to assess the robustness of the parameterization. More generally, we have shown that the model is compatible with 1.5-order PBL schemes in the WRF model, provided that prognostic TKE and eddy diffusivity are available. This compatibility suggests that the parameterization can be extended to other schemes of this class. However, its application to first-order closure PBL schemes, which do not explicitly represent TKE, remains unexplored and would likely require alternative strategies, such as enhanced eddy-diffusivity formulations, to represent turbine-induced turbulence.

8 Conclusions

Turbulent kinetic energy plays a critical role in 1.5-order PBL schemes, governing the representation of the ABL and its vertical profiles of momentum, temperature, and moisture. Introducing TKE from turbines can significantly alter this representation, particularly in scenarios involving large wind farms or wind farm clusters, emphasising the importance of accurately representing both the spatial distribution and magnitude of turbine-generated turbulence.

In this study, we present and evaluate the LKE model, a novel extension of the EWP designed to account for TKE contributions from wind turbines. A key limitation of existing mesoscale wind farm parameterizations is that TKE is injected locally at the turbine grid cells and subsequently transported downstream by advection. As a result, reproducing the downstream turbulence levels observed in LES requires an unrealistically large TKE source at the turbine locations, leading to an overestimation of TKE within the wind farm. The LKE model addresses this limitation by allowing TKE to be released progressively downstream of the turbines, thereby decoupling the location of TKE injection from the turbine position. The main improvements introduced by the LKE model are:

- The LKE model reproduces the streamwise evolution of added TKE observed in LES, with minimal TKE at the wind farm entrance, a maximum near the downstream end of the farm, and a gradual decay further downstream. The distribution and magnitude of the added TKE is directly controlled by the parameter c_λ and indirectly by σ_0 through its influence on shear generation.

https://doi.org/10.5194/egusphere-2026-2144
Preprint. Discussion started: 22 April 2026

– The injection of TKE in the LKE model is independent of TKE advection from the PBL scheme, enabling its use with other PBL schemes that lack this feature while still achieving satisfactory results regarding wind speed and TKE.

The results further demonstrate that turbine-generated TKE influences wind speed recovery within wind farms, with higher TKE levels promoting faster wake recovery. Agreement with LES-AD, in terms of wind speed deficits in the wind farm area, can be achieved without resorting to unrealistically large TKE sources, such as those required by the Fitch scheme when using 100% of the TKE source. Instead, this agreement can be obtained in the LKE model through appropriate tuning of the parameter σ_0, inherited from the EWP which controls the vertical distribution of the momentum deficit. Consequently, a combination of the parameters c_λ and σ_0 is required for each PBL scheme, as different schemes generate TKE in distinct ways and shape wind farm wakes differently. For the configurations examined in this study, we identify $\sigma_0 = 0.6\,r_0$, $1.0\,r_0$, and $1.2\,r_0$ as optimal values for the BouLac, MYJ, and MYNN PBL schemes, respectively, while maintaining $c_\lambda = 0.4$ for all cases as a baseline for future studies exploring variations in inflow wind speed, wind farm layout, and atmospheric stability.

Overall, the LKE model addresses a fundamental shortcoming of existing mesoscale wind farm parameterizations by enabling a better streamwise development of turbine-generated turbulence without overestimating TKE at the turbine locations. This improvement leads to a more realistic representation of both turbulence and wind speed deficits, while providing a flexible framework for future studies of wind farm and atmosphere interactions under different PBL schemes.

Code and data availability. The model development described in this paper consists of modifications to the Explicit Wake Parameterization (Volker et al., 2015) implemented in the WRF model version 4.2.2. The model's code is archived at [https://doi.org/10.11583/DTU.32015934] (García-Santiago, 2026). The archive contains the necessary source files with patches for the WRF model version 4.2.2 along with a concise example of input files to run the new parameterization. The current development version is also available at [https://gitlab.windenergy.dtu.dk/WRF/wrf-ewp-release] (last access: 17 Apr 2026), but the archived release linked above is the version corresponding to this manuscript. For the evaluation presented, the actuator disc and the surface fluxes routines comes from [https://doi.org/10.5281/zenodo.7765891] (Gill et al., 2023) with the associated repository [https://github.com/a2e-mmc/WRF] (last access: 17 Apr 2026). The WRF model is available for download from [https://github.com/wrf-model/WRF] (last access: 17 Apr 2026).

Appendix A: Kinetic energy budget equations under the "double averaging" approach

Double averaging, as outlined by RS1982, combines ensemble and spatial averaging of flow variables. Under this approach, an instantaneous variable, ϕ, can be separated into its ensemble mean, $\bar{\phi}$, and a fluctuating component, ϕ' ($\phi = \bar{\phi} + \phi'$). The ensemble-averaged variable, $\bar{\phi}$, is further divided into a spatial mean, $\langle\bar{\phi}\rangle$, and a spatial deviation, $\bar{\phi}''$, from this mean ($\bar{\phi} = \langle\bar{\phi}\rangle + \bar{\phi}''$). Following the double averaging approach, the spatial and ensemble-averaged total kinetic energy can be decomposed

https://doi.org/10.5194/egusphere-2026-2144
Preprint. Discussion started: 22 April 2026

in the following:

$$\frac{1}{2}\langle\overline{u_i}\,\overline{u_i}\rangle = \frac{1}{2}\langle\bar{u}_i\,\bar{u}_i\rangle + \frac{1}{2}\left\langle\overline{u_i'u_i'}\right\rangle \tag{A1}$$

$$= \frac{1}{2}\langle\bar{u}_i\rangle\langle\bar{u}_i\rangle + \frac{1}{2}\langle\bar{u}_i''\bar{u}_i''\rangle + \frac{1}{2}\left\langle\overline{u_i'u_i'}\right\rangle \tag{A2}$$

Here, the right-hand side terms in Eq. (A1) denote the spatially-averaged kinetic energy of the mean flow and the spatially-averaged turbulent kinetic energy, respectively. By further decomposing the kinetic energy of the mean flow into its spatial average and deviations, we obtain Eq. (A2) where the second term represents the heterogeneity of the mean flow in non-homogeneous conditions, as discussed by RS1982 and V2015. Following this, we focus on the derivation of budget equations for the heterogeneous mean flow component ($\frac{1}{2}\langle\bar{u}_i''\bar{u}_i''\rangle$) and the turbulent kinetic energy component ($\frac{1}{2}\langle\overline{u_i'u_i'}\rangle$). Starting from the incompressible momentum conservation:

$$\frac{\partial u_i}{\partial t} + u_j\frac{\partial u_i}{\partial x_j} = -\frac{1}{\rho}\frac{\partial p}{\partial x_i} + f_c\varepsilon_{ij3}u_j - \delta_{i3}g\frac{\theta}{\theta_0} + \nu\frac{\partial^2 u_i}{\partial x_j^2} + f_i \tag{A3}$$

where u_i is the velocity (with $i = 1,2,3$), p is the pressure, ρ is the density, f_c is the Coriolis parameter, ε_{ij3} is the Levi-Civita tensor, δ_{i3} is the Kronecker delta, g the gravitational acceleration, θ is the potential temperature with subscript 0 indicating a reference state, ν is the kinematic viscosity, and f_i is the drag force due to the turbines. Decomposing variables in Eq. (A3) using an ensemble mean and fluctuating part: $\phi = \bar{\phi} + \phi'$ ($u_i = \bar{u}_i + u_i'$, $p = \bar{p} + p'$, $\theta = \bar{\theta} + \theta'$, $f_i = \bar{f}_i + f_i'$); and taking the ensemble mean, we obtain the Reynolds-averaged Navier–Stokes (RANS) equation often used in mesoscale models:

$$\frac{\partial\bar{u}_i}{\partial t} + \bar{u}_j\frac{\partial\bar{u}_i}{\partial x_j} + \frac{\partial\overline{u_i'u_j'}}{\partial x_j} = -\frac{1}{\rho}\frac{\partial\bar{p}}{\partial x_i} + f_c\varepsilon_{ij3}\bar{u}_j - \delta_{i3}g\frac{\bar{\theta}}{\theta_0} + \nu\frac{\partial^2\bar{u}_i}{\partial x_j^2} + \bar{f}_i \tag{A4}$$

Then, we obtain the conservation equation of the perturbation u_i' by subtracting Eq. (A4) to Eq. (A3):

$$\frac{\partial u_i'}{\partial t} + \bar{u}_j\frac{\partial u_i'}{\partial x_j} + u_j'\frac{\partial\bar{u}_i}{\partial x_j} + u_j'\frac{\partial u_i'}{\partial x_j} = -\frac{1}{\rho}\frac{\partial p'}{\partial x_i} + f_c\varepsilon_{ij3}\bar{u}_j' + \delta_{i3}\frac{g\theta'}{\theta_0} + \nu\frac{\partial^2 u_i'}{\partial x_j^2} + \frac{\partial\overline{u_i'u_j'}}{\partial x_j} + f_i' \tag{A5}$$

We obtain the TKE budget equation by multiplying Eq. (A5) with u_i', taking the ensemble mean, and applying product rule:

$$\frac{\partial\frac{1}{2}\overline{u_i'u_i'}}{\partial t} + \bar{u}_j\frac{\partial\frac{1}{2}\overline{u_i'u_i'}}{\partial x_j} = -\overline{u_i'u_j'}\frac{\partial\bar{u}_i}{\partial x_j} + \delta_{i3}\frac{g}{\theta_0}\overline{u_i'\theta'} - \frac{\partial\frac{1}{2}\overline{u_i'u_i'u_j'}}{\partial x_j} - \frac{1}{\rho}\frac{\partial\overline{u_i'p'}}{\partial x_i} + \nu\overline{u_i'\frac{\partial^2 u_i'}{\partial x_j^2}} + \overline{u_i'f_i'} \tag{A6}$$

With TKE given as $k = \overline{u_i'u_i'}/2$. From Eq. (A6), all ensemble-averaged variables (e.g., $\bar{u}_i$, $\overline{u_i'u_j'}$, $\overline{u_i'\theta'}$, or $\overline{u_i'f_i'}$) are then split into a spatial mean and a spatial deviation around the mean: $\bar{\phi} = \langle\bar{\phi}\rangle + \bar{\phi}''$; followed by a spatial averaging operation. This process leads to the spatially averaged TKE budget equation:

$$\frac{\partial\langle\bar{k}\rangle}{\partial t} + \underbrace{\langle\bar{u}_j\rangle\frac{\partial\langle\bar{k}\rangle}{\partial x_j}}_{\langle\bar{\mathcal{A}}\rangle} = \underbrace{-\left\langle\overline{u_i'u_j'}\right\rangle\frac{\partial\langle\bar{u}_i\rangle}{\partial x_j}}_{\langle\bar{\mathcal{P}}_\mathrm{s}\rangle} + \underbrace{\delta_{i3}\frac{g}{\theta_0}\left\langle\overline{u_i'\theta'}\right\rangle}_{\langle\bar{\mathcal{P}}_\mathrm{b}\rangle} - \frac{\partial}{\partial x_j}\left(\underbrace{\left\langle\overline{ku_j'}\right\rangle}_{\langle\bar{\mathcal{T}}_\mathrm{t}\rangle} + \underbrace{\left\langle\overline{k}''\overline{u}_j''\right\rangle}_{\langle\bar{\mathcal{T}}_\mathrm{d}\rangle} + \underbrace{\frac{\left\langle\overline{p'u_j'}\right\rangle}{\rho}}_{\langle\bar{\mathcal{T}}_\mathrm{p}\rangle}\right)$$

$$+ \underbrace{\nu\left\langle\overline{u_i'\frac{\partial^2 u_i'}{\partial x_j^2}}\right\rangle}_{\langle\bar{\epsilon}\rangle} - \underbrace{\left\langle\overline{u_i'u_j'}''\frac{\partial\bar{u}_i''}{\partial x_j}\right\rangle}_{\langle\bar{\mathcal{P}}_\mathrm{w}\rangle} + \underbrace{\left\langle\overline{u_i'f_i'}\right\rangle}_{\langle\bar{\mathcal{P}}_\mathrm{f}\rangle} \tag{A7}$$

https://doi.org/10.5194/egusphere-2026-2144
Preprint. Discussion started: 22 April 2026

For the heterogeneous mean flow component budget, one can derive it by first obtaining the spatially averaged RANS equation by splitting ensemble-averaged terms ($\bar{\phi} = \langle\bar{\phi}\rangle + \bar{\phi}''$) in Eq. (A4) and then applying spatial averaging

$$\frac{\partial \langle\bar{u}_i\rangle}{\partial t} + \langle\bar{u}_j\rangle \frac{\partial \langle\bar{u}_i\rangle}{\partial x_j} + \frac{\partial \left\langle \overline{u_i' u_j'} \right\rangle}{\partial x_j} + \frac{\partial \langle \bar{u}_i'' \bar{u}_j'' \rangle}{\partial x_j} = -\frac{1}{\rho}\frac{\partial \langle\bar{p}\rangle}{\partial x_i} + f_c \varepsilon_{ij3} \langle\bar{u}_j\rangle - \delta_{i3} g \frac{\langle\bar{\theta}\rangle}{\theta_0} + \nu \frac{\partial^2 \langle\bar{u}_i\rangle}{\partial x_j^2} + \langle\bar{f}_i\rangle \tag{A8}$$

Then, subtracting Eq. (A8) to Eq. (A4) and applying the product rule, we can obtain a conservation equation for $\bar{u}_i''$:

$$\frac{\partial \bar{u}_i''}{\partial t} + \langle\bar{u}_j\rangle \frac{\partial \bar{u}_i''}{\partial x_j} - \frac{\partial \overline{u_i' u_j'}''}{\partial x_j} + \frac{\partial}{\partial x_j}\left(\langle\bar{u}_i\rangle \bar{u}_j'' + \bar{u}_i'' \bar{u}_j'' - \langle \bar{u}_i'' \bar{u}_j'' \rangle\right) = -\frac{1}{\rho}\frac{\partial \bar{p}''}{\partial x_i} + f_c \varepsilon_{ij3} \bar{u}_j'' - \delta_{i3} g \frac{\bar{\theta}''}{\theta_0} + \nu \frac{\partial^2 \bar{u}_i''}{\partial x_j^2} + \bar{f}_i'' \tag{A9}$$

Multiplying Eq. (A9) with $\bar{u}_i''$ and then applying a spatial average, we obtain the LKE budget equation:

$$\begin{aligned}
\frac{\partial \frac{1}{2}\langle \bar{u}_i'' \bar{u}_i'' \rangle}{\partial t} = & \underbrace{-\langle\bar{u}_j\rangle \frac{\partial \frac{1}{2}\langle \bar{u}_i'' \bar{u}_i'' \rangle}{\partial x_j}}_{\langle\bar{\mathcal{A}}_\mathrm{d}\rangle} \underbrace{-\langle \bar{u}_i'' \bar{u}_j'' \rangle \frac{\partial \langle\bar{u}_i\rangle}{\partial x_j}}_{\langle\bar{\mathcal{P}}_\mathrm{d}\rangle} \underbrace{+\left\langle \overline{u_i' u_j'}'' \frac{\partial \bar{u}_i''}{\partial x_j} \right\rangle}_{\langle\bar{\mathcal{P}}_\mathrm{w}\rangle} \\
& \underbrace{-\frac{\partial}{\partial x_j}\left(\left\langle \bar{u}_i'' \overline{u_i' u_j'}'' \right\rangle + \frac{\langle \bar{u}_i'' \bar{u}_i'' \bar{u}_j'' \rangle}{2} \right)}_{\langle\bar{\mathcal{T}}_\mathrm{d}\rangle} \underbrace{-\left\langle \frac{\bar{u}_i''}{\rho} \frac{\partial \bar{p}''}{\partial x_i} \right\rangle}_{\langle\bar{\mathcal{C}}_\mathrm{d}\rangle} \\
& \underbrace{-\delta_{i3} \frac{g}{\theta_0} \langle \bar{u}_i'' \bar{\theta}'' \rangle}_{\langle\bar{\mathcal{B}}_\mathrm{d}\rangle} \underbrace{+\nu \left\langle \bar{u}_i'' \frac{\partial^2 \bar{u}_i''}{\partial x_j \partial x_j} \right\rangle}_{\langle\bar{\mathcal{D}}_\nu\rangle} \underbrace{+\langle \bar{u}_i'' \bar{f}_i'' \rangle}_{\langle\bar{\mathcal{F}}_\mathrm{d}\rangle},
\end{aligned} \tag{A10}$$

Notice that in RS1982 the term $\langle\bar{\mathcal{F}}_\mathrm{d}\rangle$ is represented by the term $\frac{1}{\rho}\langle\bar{u}_i\rangle \left\langle \frac{\partial \bar{p}''}{\partial x_i} \right\rangle$, a pressure drag form multiplied by the mean velocity which obtained from the term $\frac{1}{\rho}\left\langle \bar{u}_i'' \frac{\partial \bar{p}''}{\partial x_i} \right\rangle$.

One could argue that the averaging in Eqs. (A7) involves both a moving average (following the flow) and a spatial average, which could directly impact the advective terms (and indirectly the production and transport), due to the derivative and averaging operators not exactly commuting. However, this commutation error is assumed small, as done in RS1982 and similar studies following it; if the grid spacing were much smaller this could introduce additional uncertainty, but such grid spacings ($\Delta x \sim D$) would introduce other problems into this mesoscale parameterization.

Appendix B: Intercomparison of inflow conditions

We compare the inflow conditions (i.e., simulations without the wind farm) of the simulated neutral atmosphere from mesoscale simulations using MYNN, MYJ, and BouLac PBL schemes, with LES as the reference. Figure B1 showcases the inflow vertical profiles of horizontal wind speed, wind direction, TKE, and momentum eddy-diffusivity, averaged over the last simulation hour (Table 1) and the horizontal computational domain, from both LES and mesoscale simulations. In this comparison, MYNN's representation in Fig. B1 has TKE advection deactivated, given that both activated and deactivated options yield similar inflow conditions.

https://doi.org/10.5194/egusphere-2026-2144
Preprint. Discussion started: 22 April 2026

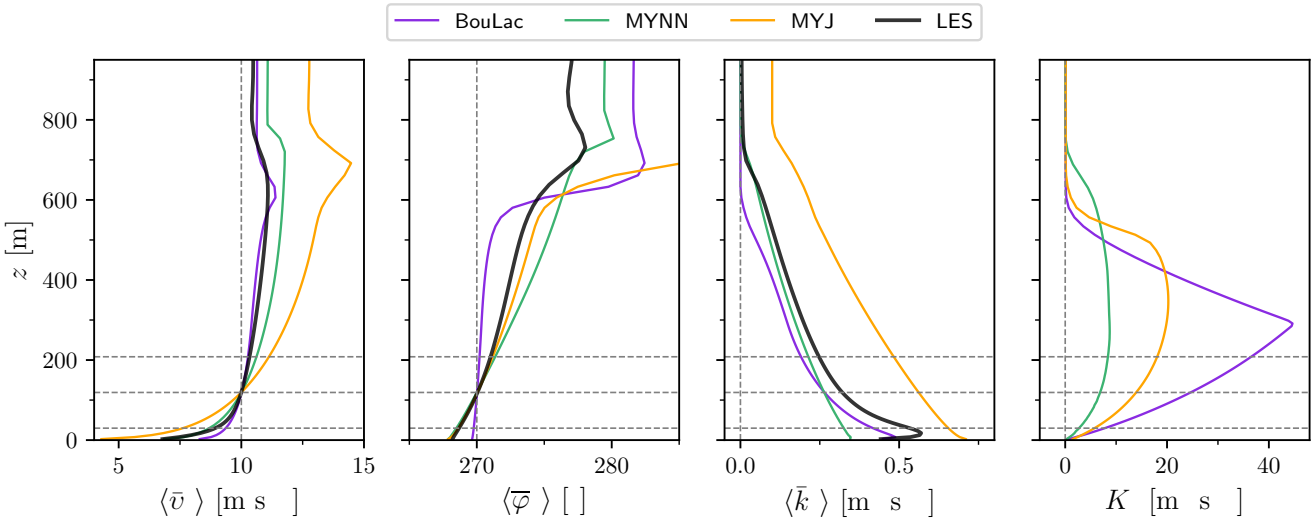

Figure B1. Time-averaged vertical profiles of (a) horizontal wind speed, (b) wind direction, (c) TKE, and (d) momentum eddy-diffusivity, comparing mesoscale simulations using MYNN, MYJ, and BouLac PBL schemes against LES for the simulated neutral atmosphere. Profiles represent spatial averages over the proposed wind farm area (Fig. 2), with horizontal grey lines indicating the wind turbine rotor's top, bottom, and hub heights.

For wind speed profiles (Fig. B1a), BouLac's simulation aligns more with the LES outcome, whereas MYJ shows the greatest deviation. Specifically, MYJ predicts the sharpest wind speed gradient at the rotor area, unlike BouLac, which predicts the least. Surface wind speeds are lowest with MYJ (4 m s^{-1}) and highest with BouLac (8 m s^{-1}), with LES reporting a surface wind speed of 7 m s^{-1}. In this context, MYNN's performance is intermediate between BouLac's and MYJ's. The jet peak is located in the 600 m to 750 m layer for all models. In terms of wind veer (Fig. B1b), all simulations except BouLac exhibit comparable profiles at the rotor area but diverge at higher altitudes, with the most notable differences occurring at the boundary layer top (600 m to 750 m layer). BouLac's wind direction profile remains constant at 270° from the surface to the rotor top.

TKE profiles (Fig. B1c) from all simulations consistently show the highest production at the surface, decreasing to zero or a constant value at their boundary layer top. TKE at hub height is similar for MYNN and BouLac (0.25 m^2 s^{-2}), higher for LES (0.4 m^2 s^{-2}), and highest for MYJ (5.5 m^2 s^{-2}), with MYJ imposing a constant value of 0.1 m^2 s^{-2} above the boundary layer height. Momentum eddy-diffusivity (K_m) profiles (Fig. B1d) vary across the PBL schemes, with BouLac presenting the highest values and MYNN the lowest within the boundary layer. Additionally, the profile shapes differ, with BouLac exhibiting sharp gradients with a peak at 250 m, contrasting with the smoother profiles of MYNN and MYJ.

In summary, LES and mesoscale simulations with the three PBL schemes show generally consistent wind speed and direction profiles within the rotor area, achieving uniform hub-height wind speed and direction (10 m s^{-1} and 270°). However, variations in TKE profiles, shear, and veer across the boundary layer underscore the impacts of employing different PBL schemes under nearly identical conditions (see Table 1).

https://doi.org/10.5194/egusphere-2026-2144
Preprint. Discussion started: 22 April 2026

Appendix C: Turbine-induced LKE source

We follow the procedure from Abkar and Porté-Agel (2015) to get the source term $\langle \bar{u}_i'' \bar{f}_i'' \rangle$, but with the difference that in our notation, the double-primes denote only the spatial deviation from the mean, but in Abkar and Porté-Agel (2015), denotes spatial and ensemble deviation. We define two averaged areas: The horizontal grid cell area, defined by the model's grid spacing $A = \Delta y \times \Delta x$, and a relatively smaller area δa (inside A) enclosing the wind turbines. We assume that each wind turbine force $\bar{f}_{wt,i}$ is smeared out over δa and outside it is zero. Then, the total spatially averaged force over the grid-cell A is:

$$\langle \bar{f}_i \rangle = \frac{1}{A} \sum_{n=1}^{N_{wt}} \bar{f}_{wt,i} \delta_A \approx \frac{\delta_A N_{wt}}{A} \bar{f}_{wt,i} \tag{C1}$$

where N_{wt} is the number of wind turbines in A. The right-hand side of Eq. (C1) assumes that all wind turbines impose the same drag force. In reality, if there is more than one wind turbine inside the grid cell, $\bar{f}_{wt,i}$ might differ for each turbine due to sub-grid wake interactions. Future iterations of the model should account for that behaviour.

For the horizontal wind, we used the rotor-averaged wind speed $\bar{u}_{wt,i}$ inside δa and $\bar{u}_i$ outside of it. With the definitions of the horizontal wind and force inside A and δa, and using spatial decomposition ($\bar{\phi}'' = \bar{\phi} - \langle \bar{\phi} \rangle$), gives the following:

$$\begin{aligned}
\langle \bar{u}_i'' \bar{f}_i'' \rangle &= \frac{1}{A} \int_A \bar{u}_i'' \bar{f}_i'' dA, \qquad \text{(C2)} \\
&= \frac{1}{A} \int_{A - N_{wt}\delta_A} \bar{u}_i'' \bar{f}_i'' dA + \frac{N_{wt}}{A} \int_{\delta_A} \bar{u}_i'' \bar{f}_i'' dA, \\
&= \frac{1}{A} \int_{A - N_{wt}\delta_A} \left(\bar{u}_i - \langle \bar{u}_i \rangle\right) \left(-\langle \bar{f}_i \rangle\right) dA + \frac{N_{wt}}{A} \int_{\delta_A} \left(\bar{u}_{wt,i} - \langle \bar{u}_i \rangle\right) \langle \bar{f}_i \rangle \left(\frac{A}{\delta_A N_{wt}} - 1 \right) dA, \\
&= -\langle \bar{f}_i \rangle \left(\langle \bar{u}_i \rangle - \bar{u}_{wt,i} \right). \qquad \text{(C3)}
\end{aligned}$$

Similarly, as in V2015, we use the grid-cell-averaged speed at hub height $\langle \bar{v}_h \rangle$ as the inflow velocity $\bar{u}_0$. Then, we can approximate $\bar{u}_{wt,i} = \bar{u}_0(1 - a_x)$, leaving Eq. C3 as :

$$\langle \bar{u}'' \bar{f}'' \rangle = -\langle \bar{f} \rangle \langle \bar{v}_h \rangle \left(1 - (1 - a_x)\right), \tag{C4}$$

where the grid-cell-averaged force,$\langle \bar{f} \rangle$, comes from V2015:

$$\langle \bar{f} \rangle = -N_{wt} \sqrt{\frac{\pi}{8}} \frac{r_0^2 C_{\mathrm{T}} \langle \bar{v}_h \rangle^2}{A\, \sigma_{\mathrm{e}}} \exp\left[-\frac{1}{2} \left(\frac{z - h}{\sigma_{\mathrm{e}}} \right)^2 \right], \tag{C5}$$

with the effective length scale, σ_{e} in Eq. (C5) controlling the wake expansion.

Appendix D: LES grid resolution

The representation of turbulent structures in LES is influenced by various factors, including atmospheric stability and grid size (Pope, 2004; Wurps et al., 2020; Sanchez Gomez et al., 2023). We compare our LES results to that of GS2024, which shares

https://doi.org/10.5194/egusphere-2026-2144
Preprint. Discussion started: 22 April 2026

the same model configurations except horizontal grid spacing and domain size, where we use 20 m compared to their 10 m resolution.

The chosen grid spacing of 20 m proves sufficient for simulating a neutral atmospheric boundary layer and assessing wind farm parameterizations. This is evidenced by our analysis of the total turbulence kinetic energy ($\bar{k}_{\mathrm{tot}}$), which integrates the resolved ($\bar{k}_{\mathrm{res}}$) and sub-grid scale ($\bar{k}_{\mathrm{sgs}}$) contributions. Although the resolved TKE at the rotor area is slightly lower in our 20-meter simulation (about 2.2 %) compared to the 10-meter setup, both configurations effectively resolve over 85 % of the total TKE within and above the rotor area (Fig. D1a). This value meets the criteria of > 80 % for a well-resolved flow (Pope, 2004). Moreover, both simulations display comparable total TKE profiles, with the most noticeable differences in the surface layer, where sub-grid scale contributions are predominant (Fig. D1b).

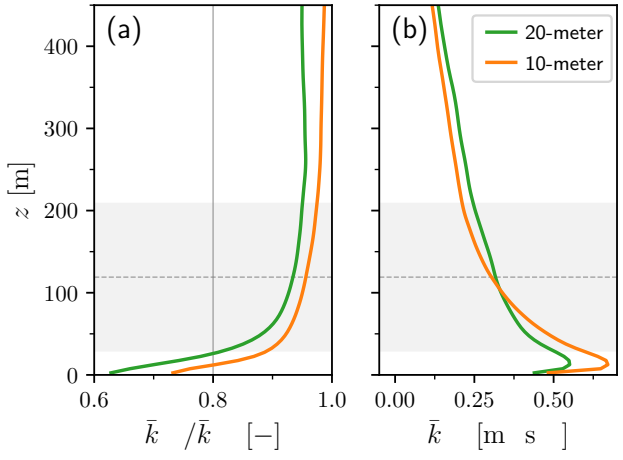

Figure D1. Vertical profiles of (a) fraction of resolved TKE and (b) total TKE from simulations of a neutral atmosphere using WRF-LES with horizontal grid spacings of 10 m (used in GS2024) and 20 m (used in this study). Profiles represent a 1-kilometre area at the centre of the LES domains. For reference, the vertical solid and horizontal dashed grey lines correspond to 80 % of resolved TKE and the hub height, respectively, with the grey-shaded area corresponding to the turbine rotor.

Author contributions. OGS implemented and improved the new model, wrote the first draft, carried out the experiments and analysed the results. SO and PV conceptualised the idea for the model and made the first implementations. MK added descriptions about scaling/dependence from PBL schemes. All authors participated in the analysis design and the manuscript's writing and editing.

Competing interests. The authors declare no competing interests to declare.

https://doi.org/10.5194/egusphere-2026-2144
Preprint. Discussion started: 22 April 2026

Acknowledgements. OGS and JB acknowledge the support of the European Union Horizon 2020 research and innovation programme under grant agreement no. 861291 as part of the Train2Wind Marie Skłodowska-Curie Innovative Training Network (https://www.train2wind.eu/). OGS and JB further acknowledge partial funding from the Clean Energy Transition Partnership (CETPartnership) under the 2023 joint call for research proposals. CETPartnership is co-funded by the European Commission under grant agreement no. 101069750, together with the national and regional funding organisations listed at https://cetpartnership.eu/funding-agencies-and-call-modules. AH was partially funded by the Independent Research Fund Denmark through the Multi-scale Atmospheric Modeling Above the Seas (MAMAS) project. The authors thank Jeffrey Mirocha at Lawrence Livermore National Laboratory for helpful discussions around the actuator-disc implementation. We also acknowledge the computational resources provided by the Sophia HPC Cluster at the Technical University of Denmark, DOI: https://doi.org/10.57940/FAFC-6M81.

https://doi.org/10.5194/egusphere-2026-2144
Preprint. Discussion started: 22 April 2026

References

Abkar, M. and Porté-Agel, F.: A New Wind-Farm Parameterization for Large-Scale Atmospheric Models, J. Renew. and Sust. Energ., 7, 013 121, https://doi.org/10.1063/1.4907600, 2015.

Akhtar, N., Geyer, B., Rockel, B., Sommer, P. S., and Schrum, C.: Accelerating Deployment of Offshore Wind Energy Alter Wind Climate and Reduce Future Power Generation Potentials, Sci Rep, 11, 11 826, https://doi.org/10.1038/s41598-021-91283-3, 2021.

Ali, K., Schultz, D. M., Revell, A., Stallard, T., and Ouro, P.: Assessment of Five Wind-Farm Parameterizations in the Weather Research and Forecasting Model: A Case Study of Wind Farms in the North Sea, Mon. Wea. Rev., 151, 2333–2359, https://doi.org/10.1175/MWR-D-23-0006.1, 2023.

Allaerts, D. and Meyers, J.: Boundary-Layer Development and Gravity Waves in Conventionally Neutral Wind Farms, J. Fluid Mech., 814, 95–130, https://doi.org/10.1017/jfm.2017.11, 2017.

Archer, C. L., Wu, S., Ma, Y., and Jiménez, P. A.: Two Corrections for Turbulent Kinetic Energy Generated by Wind Farms in the WRF Model, Mon. Wea. Rev., 148, 4823–4835, https://doi.org/10.1175/MWR-D-20-0097.1, 2020.

Bak, C., Zahle, F., Bitsche, R., Kim, T., Yde, A., Henriksen, L. C., Hansen, M. H., Blasques, J. P. A. A., Gaunaa, M., and Natarajan, A.: The DTU 10-MW Reference Wind Turbine, Tech. rep., DTU Wind Energy, 2013.

Banerjee, T., Roo, F. D., and Mauder, M.: Connecting the Failure of K Theory inside and above Vegetation Canopies and Ejection–Sweep Cycles by a Large-Eddy Simulation, Journal of Applied Meteorology and Climatology, 56, 3119–3131, https://doi.org/10.1175/JAMC-D-16-0363.1, 2017.

Bodini, N., Optis, M., Redfern, S., Rosencrans, D., Rybchuk, A., Lundquist, J. K., Pronk, V., Castagneri, S., Purkayastha, A., Draxl, C., Krishnamurthy, R., Young, E., Roberts, B., Rosenlieb, E., and Musial, W.: The 2023 National Offshore Wind Data Set (NOW-23), Earth Syst. Sci. Data, pp. 1–57, https://doi.org/10.5194/essd-2023-490, 2023.

Bougeault, P. and Lacarrere, P.: Parameterization of Orography-Induced Turbulence in a Mesobeta–Scale Model, Mon. Wea. Rev., 117, 1872–1890, https://doi.org/10.1175/1520-0493(1989)117<1872:POOITI>2.0.CO;2, 1989.

Brunet, Y.: Turbulent Flow in Plant Canopies: Historical Perspective and Overview, Boundary-Layer Meteorol, 177, 315–364, https://doi.org/10.1007/s10546-020-00560-7, 2020.

Carvalho, D., Rocha, A., Gómez-Gesteira, M., and Silva Santos, C.: Sensitivity of the WRF Model Wind Simulation and Wind Energy Production Estimates to Planetary Boundary Layer Parameterizations for Onshore and Offshore Areas in the Iberian Peninsula, Applied Energy, 135, 234–246, https://doi.org/10.1016/j.apenergy.2014.08.082, 2014.

Deardorff, J. W.: Stratocumulus-Capped Mixed Layers Derived from a Three-Dimensional Model, Boundary-Layer Meteorol, 18, 495–527, https://doi.org/10.1007/BF00119502, 1980.

Dellwik, E., van der Laan, M. P., Angelou, N., Mann, J., and Sogachev, A.: Observed and Modeled Near-Wake Flow behind a Solitary Tree, Agricultural and Forest Meteorology, 265, 78–87, https://doi.org/10.1016/j.agrformet.2018.10.015, 2019.

Draxl, C., Hahmann, A. N., Peña, A., and Giebel, G.: Evaluating Winds and Vertical Wind Shear from Weather Research and Forecasting Model Forecasts Using Seven Planetary Boundary Layer Schemes, Wind Energy, 17, 39–55, https://doi.org/10.1002/we.1555, 2014.

Finnigan, J.: Turbulence in Plant Canopies, Annual Review of Fluid Mechanics, 32, 519–571, https://doi.org/10.1146/annurev.fluid.32.1.519, 2000.

Finnigan, J. J. and Shaw, R. H.: Double-Averaging Methodology and Its Application to Turbulent Flow in and above Vegetation Canopies, Acta Geophys., 56, 534–561, https://doi.org/10.2478/s11600-008-0034-x, 2008.

https://doi.org/10.5194/egusphere-2026-2144
Preprint. Discussion started: 22 April 2026

Fischereit, J., Brown, R., Larsén, X. G., Badger, J., and Hawkes, G.: Review of Mesoscale Wind-Farm Parametrizations and Their Applications, Boundary-Layer Meteorol, 182, 175–224, https://doi.org/10.1007/s10546-021-00652-y, 2022.

Fitch, A. C., Olson, J. B., Lundquist, J. K., Dudhia, J., Gupta, A. K., Michalakes, J., and Barstad, I.: Local and Mesoscale Impacts of Wind Farms as Parameterized in a Mesoscale NWP Model, Mon. Wea. Rev., 140, 3017–3038, https://doi.org/10.1175/MWR-D-11-00352.1, 2012.

Floors, R., Hahmann, A. N., and Peña, A.: Evaluating Mesoscale Simulations of the Coastal Flow Using Lidar Measurements, J. Geophys. Res.-Atmos., 123, 2718–2736, https://doi.org/10.1002/2017JD027504, 2018.

García-Santiago, O.: Source-Code for "A Wind-Farm Wake-Turbulence Parameterization for the WRF Model (EWP v2.0)", Technical University of Denmark, https://doi.org/10.11583/DTU.32015934.v1, 2026.

García-Santiago, O., Hahmann, A. N., Badger, J., and Peña, A.: Evaluation of Wind Farm Parameterizations in the WRF Model under Different Atmospheric Stability Conditions with High-Resolution Wake Simulations, Wind Energy Science, 9, 963–979, https://doi.org/10.5194/wes-9-963-2024, 2024.

Gill, D., dudhia, weiwangncar, Peckham, S., Bresch, J., Kavulich, M., Black, T., Carson, L., smileMchen, Zhang, X., Werner, K., Hawbecker, P., huangwei5934, Manning, K., Duda, M., stacywalters, Liu, Z. J., Barlage, M., bonnland, Quon, E., Olson, J., Göbel, M., kayeekayee, gthompsnWRF, Sauer, J., Jha, P., Juliano, T., Guerrette, J. J., pedro-jm, and domingom: A2e-Mmc/WRF: End of A2e MMC Project, Zenodo, https://doi.org/10.5281/zenodo.7765891, 2023.

Hahmann, A. N., Sīle, T., Witha, B., Davis, N. N., Dörenkämper, M., Ezber, Y., García-Bustamante, E., González-Rouco, J. F., Navarro, J., Olsen, B. T., and Söderberg, S.: The Making of the New European Wind Atlas – Part 1: Model Sensitivity, Geosci Model Dev., 13, 5053–5078, https://doi.org/10.5194/gmd-13-5053-2020, 2020.

Janjić, Z. I.: The Step-Mountain Coordinate: Physical Package, Mon. Wea. Rev., 118, 1429–1443, https://doi.org/10.1175/1520-0493(1990)118<1429:TSMCPP>2.0.CO;2, 1990.

Janjić, Z. I.: Nonsingular Implementation of the Mellor-Yamada Level 2.5 Scheme in the NCEP Meso Model, Tech. rep., 2001.

Jiménez, P. A., Dudhia, J., González-Rouco, J. F., Navarro, J., Montávez, J. P., and García-Bustamante, E.: A Revised Scheme for the WRF Surface Layer Formulation, Mon. Wea. Rev., 140, 898–918, https://doi.org/10.1175/MWR-D-11-00056.1, 2012.

Juliano, T. W., Kosović, B., Jiménez, P. A., Eghdami, M., Haupt, S. E., and Martilli, A.: "Gray Zone" Simulations Using a Three-Dimensional Planetary Boundary Layer Parameterization in the Weather Research and Forecasting Model, Mon. Wea. Rev., 150, 1585–1619, https://doi.org/10.1175/MWR-D-21-0164.1, 2022.

Katul, G. G., Cava, D., Siqueira, M., and Poggi, D.: Scalar Turbulence within the Canopy Sublayer, in: Coherent Flow Structures at Earth's Surface, chap. 6, pp. 73–95, John Wiley & Sons, Ltd, ISBN 978-1-118-52722-1, https://doi.org/10.1002/9781118527221.ch6, 2013.

Kosović, B., Munoz, P. J., Juliano, T. W., Martilli, A., Eghdami, M., Barros, A. P., and Haupt, S. E.: Three-Dimensional Planetary Boundary Layer Parameterization for High-Resolution Mesoscale Simulations, in: Journal of Physics: Conference Series, vol. 1452, p. 012080, IOP Publishing, https://doi.org/10.1088/1742-6596/1452/1/012080, 2020.

Lanzilao, L. and Meyers, J.: Effects of Self-Induced Gravity Waves on Finite Wind-Farm Operations Using a Large-Eddy Simulation Framework, J. Phys.: Conf. Ser., 2265, 022 043, https://doi.org/10.1088/1742-6596/2265/2/022043, 2022.

Larsén, X. G. and Fischereit, J.: A Case Study of Wind Farm Effects Using Two Wake Parameterizations in the Weather Research and Forecasting (WRF) Model (V3.7.1) in the Presence of Low-Level Jets, Geosci Model Dev., 14, 3141–3158, https://doi.org/10.5194/gmd-14-3141-2021, 2021.

https://doi.org/10.5194/egusphere-2026-2144
Preprint. Discussion started: 22 April 2026

Lu, J., Nazarian, N., Hart, M. A., Krayenhoff, E. S., and Martilli, A.: A One-Dimensional Urban Flow Model with an Eddy-Diffusivity Mass-Flux (EDMF) Scheme and Refined Turbulent Transport (MLUCM v3.0), Geoscientific Model Development, 17, 2525–2545, https://doi.org/10.5194/gmd-17-2525-2024, 2024.

Lundquist, J. K., DuVivier, K. K., Kaffine, D., and Tomaszewski, J. M.: Costs and Consequences of Wind Turbine Wake Effects Arising from Uncoordinated Wind Energy Development, Nat. Energy, 4, 26–34, https://doi.org/10.1038/s41560-018-0281-2, 2019.

Ma, Y., Archer, C. L., and Vasel-Be-Hagh, A.: The Jensen Wind Farm Parameterization, Wind Energy Science, 7, 2407–2431, https://doi.org/10.5194/wes-7-2407-2022, 2022.

Maas, O. and Raasch, S.: Wake Properties and Power Output of Very Large Wind Farms for Different Meteorological Conditions and Turbine Spacings: A Large-Eddy Simulation Case Study for the German Bight, Wind Energy Science, 7, 715–739, https://doi.org/10.5194/wes-7-715-2022, 2022.

Mellor, G. L. and Yamada, T.: Development of a Turbulence Closure Model for Geophysical Fluid Problems, Reviews of Geophysics, 20, 851–875, https://doi.org/10.1029/RG020i004p00851, 1982.

Mirocha, J. D., Kosovic, B., Aitken, M. L., and Lundquist, J. K.: Implementation of a Generalized Actuator Disk Wind Turbine Model into the Weather Research and Forecasting Model for Large-Eddy Simulation Applications, J. Renew. and Sust. Energ., 6, 013 104, https://doi.org/10.1063/1.4861061, 2014.

Nakanishi, M. and Niino, H.: Development of an Improved Turbulence Closure Model for the Atmospheric Boundary Layer, J. Meteorol. Soc. Jpn. Ser. II, 87, 895–912, https://doi.org/10.2151/jmsj.87.895, 2009.

Nazarian, N., Krayenhoff, E. S., and Martilli, A.: A One-Dimensional Model of Turbulent Flow through "Urban" Canopies (MLUCM v2.0): Updates Based on Large-Eddy Simulation, Geoscientific Model Development, 13, 937–953, https://doi.org/10.5194/gmd-13-937-2020, 2020.

Olsen, B. T., Hahmann, A. N., Sempreviva, A. M., Badger, J., and Jørgensen, H. E.: An Intercomparison of Mesoscale Models at Simple Sites for Wind Energy Applications, Wind Energy Science, 2, 211–228, https://doi.org/10.5194/wes-2-211-2017, 2017.

Pan, Y. and Archer, C. L.: A Hybrid Wind-Farm Parametrization for Mesoscale and Climate Models, Boundary-Layer Meteorol, 168, 469–495, https://doi.org/10.1007/s10546-018-0351-9, 2018.

Peña, A., Mirocha, J. D., and Paul van der Laan, M.: Evaluation of the Fitch Wind-Farm Wake Parameterization with Large-Eddy Simulations of Wakes Using the Weather Research and Forecasting Model, Mon. Wea. Rev., 150, 3051–3064, https://doi.org/10.1175/MWR-D-22-0118.1, 2022.

Peña, A., García-Santiago, O., Kosović, B., Mirocha, J. D., and Juliano, T. W.: Can We yet Do a Fairer and More Complete Validation of Wind Farm Parametrizations in the WRF Model?, in: Journal of Physics: Conference Series, vol. 2505, p. 012024, https://doi.org/10.1088/1742-6596/2505/1/012024, 2023.

Pope, S. B.: Ten Questions Concerning the Large-Eddy Simulation of Turbulent Flows, New J. Phys., 6, 35, https://doi.org/10.1088/1367-2630/6/1/035, 2004.

Porté-Agel, F., Bastankhah, M., and Shamsoddin, S.: Wind-Turbine and Wind-Farm Flows: A Review, Boundary-Layer Meteorol, 174, 1–59, https://doi.org/10.1007/s10546-019-00473-0, 2020.

Pryor, S. C., Barthelmie, R. J., Shepherd, T. J., Hahmann, A. N., and Santiago, O. M. G.: Wakes in and between Very Large Offshore Arrays, J. Phys.: Conf. Ser., 2265, 022 037, https://doi.org/10.1088/1742-6596/2265/2/022037, 2022.

Raupach, M. R. and Shaw, R. H.: Averaging Procedures for Flow within Vegetation Canopies, Boundary-Layer Meteorol, 22, 79–90, https://doi.org/10.1007/BF00128057, 1982.

https://doi.org/10.5194/egusphere-2026-2144
Preprint. Discussion started: 22 April 2026

Rybchuk, A., Juliano, T. W., Lundquist, J. K., Rosencrans, D., Bodini, N., and Optis, M.: The Sensitivity of the Fitch Wind Farm Parameterization to a Three-Dimensional Planetary Boundary Layer Scheme, Wind Energy Science, 7, 2085–2098, https://doi.org/10.5194/wes-7-2085-2022, 2022.

Sanchez Gomez, M., Lundquist, J. K., Mirocha, J. D., and Arthur, R. S.: Investigating the Physical Mechanisms That Modify Wind Plant Blockage in Stable Boundary Layers, Wind Energy Science, 8, 1049–1069, https://doi.org/10.5194/wes-8-1049-2023, 2023.

Santiago, J. L. and Martilli, A.: A Dynamic Urban Canopy Parameterization for Mesoscale Models Based on Computational Fluid Dynamics Reynolds-Averaged Navier–Stokes Microscale Simulations, Boundary-Layer Meteorol, 137, 417–439, https://doi.org/10.1007/s10546-010-9538-4, 2010.

Sanz, C.: A Note on k - ε Modelling of Vegetation Canopy Air-Flows, Boundary-Layer Meteorology, 108, 191–197, https://doi.org/10.1023/A:1023066012766, 2003.

Shen, W. Z., Mikkelsen, R., Sørensen, J. N., and Bak, C.: Tip Loss Corrections for Wind Turbine Computations, Wind Energy, 8, 457–475, https://doi.org/10.1002/we.153, 2005.

Shepherd, T. J., Barthelmie, R. J., and Pryor, S. C.: Sensitivity of Wind Turbine Array Downstream Effects to the Parameterization Used in WRF, J. Appl. Meteorol. Clim., 59, 333–361, https://doi.org/10.1175/JAMC-D-19-0135.1, 2020.

Siedersleben, S. K., Platis, A., Lundquist, J. K., Djath, B., Lampert, A., Bärfuss, K., Cañadillas, B., Schulz-Stellenfleth, J., Bange, J., Neumann, T., and Emeis, S.: Turbulent Kinetic Energy over Large Offshore Wind Farms Observed and Simulated by the Mesoscale Model WRF (3.8.1), Geosci Model Dev., 13, 249–268, https://doi.org/10.5194/gmd-13-249-2020, 2020.

Skamarock, C., Klemp, B., Dudhia, J., Gill, O., Liu, Z., Berner, J., Wang, W., Powers, G., Duda, G., Barker, D., and Huang, X.-y.: A Description of the Advanced Research WRF Model Version 4.3, Tech. Rep. NCAR/TN-556+STR), NCAR/UCAR, 2021.

Skamarock, W. C.: Evaluating Mesoscale NWP Models Using Kinetic Energy Spectra, Mon. Wea. Rev., 132, 3019–3032, https://doi.org/10.1175/MWR2830.1, 2004.

Sogachev, A., Kelly, M., and Leclerc, M. Y.: Consistent Two-Equation Closure Modelling for Atmospheric Research: Buoyancy and Vegetation Implementations, Boundary-Layer Meteorol, 145, 307–327, https://doi.org/10.1007/s10546-012-9726-5, 2012.

van der Laan, M. P., Baungaard, M., and Kelly, M.: Brief Communication: A Clarification of Wake Recovery Mechanisms, Wind Energy Science, 8, 247–254, https://doi.org/10.5194/wes-8-247-2023, 2023.

Veers, P., Dykes, K., Lantz, E., Barth, S., Bottasso, C. L., Carlson, O., Clifton, A., Green, J., Green, P., Holttinen, H., Laird, D., Lehtomäki, V., Lundquist, J. K., Manwell, J., Marquis, M., Meneveau, C., Moriarty, P., Munduate, X., Muskulus, M., Naughton, J., Pao, L., Paquette, J., Peinke, J., Robertson, A., Sanz Rodrigo, J., Sempreviva, A. M., Smith, J. C., Tuohy, A., and Wiser, R.: Grand Challenges in the Science of Wind Energy, Science, 366, eaau2027, https://doi.org/10.1126/science.aau2027, 2019.

Volker, P. J., Badger, J., Hahmann, A. N., and Ott, S.: The Explicit Wake Parametrisation V1.0: A Wind Farm Parametrisation in the Mesoscale Model WRF, Geosci Model Dev., 8, 3715–3731, https://doi.org/10.5194/gmd-8-3715-2015, 2015.

Wurps, H., Steinfeld, G., and Heinz, S.: Grid-Resolution Requirements for Large-Eddy Simulations of the Atmospheric Boundary Layer, Boundary-Layer Meteorol, 175, 179–201, https://doi.org/10.1007/s10546-020-00504-1, 2020.

Wyngaard, J. C.: Atmospheric Turbulence, Annual Review of Fluid Mechanics, 24, 205–234, https://doi.org/10.1146/annurev.fl.24.010192.001225, 1992.

Wyngaard, J. C.: Turbulence in the Atmosphere, Cambridge University Press, Cambridge, ISBN 978-0-521-88769-4, https://doi.org/10.1017/CBO9780511840524, 2010.